Tunable Fano Resonance in Al-Ag Plasmonic Nanorod

Supervisor:

Avijit Das

Submitted by:

Nafi Khan- 12221084

Rownak Nowrin Haque- 13110038

Lubaba Mashiat Ali- 13121102

Rifat Jahan- 13121060

Submitted to the Department of Electrical and Electronics Engineering, BRAC University

In partial fulfillment of the requirements for the degree of Bachelor of Science
April 2017

Abstract

Colloidal nanoparticles have unique Localized Surface Plasmon Resonance (LSPR) properties. There are various applications for LSPR in optics, photo catalysis and photovoltaic. Recently LSPR has been critically acclaimed as a biomolecule detection method. We investigate the unique plasmonic behavior of heterogeneous Al-Ag nanorod dimers. The LSPR behavior of this structure shows a significant Fano dip in its absorption cross section spectrum. This fano resonance can be tuned both in wavelength and amplitude by varying nanorod dimensions, separation distance and refractive index of the surrounding environment. We try to find the most sensitive configuration within these variables. The Al-Ag nanorod plasmonic structure shows a high sensitivity of 295~297.5 to the surrounding environment. This proves it as an excellent applicant for sensing and detecting biomarkers of different diseases and thus accelerating medical diagnostics technology.

1. Introduction

Nanoparticle has properties and capabilities that are all unique from each other, depending onthe material type. This makes them very interesting in a number of ways giving researchers opportunities to research more and more as they come to great use. From developing field of solar technology to medical uses the key factor has been cost efficiency which is also leading to creating newer technology. Alongside, Localized Surface Plasmon Resonance (LSPR) has been a topic of interest among many researchers over the past few years.

1.1 Nanoplasmonics

The existence of surface plasmons was first discovered by Rufus Ritchie in 1957. This was followed by almost two decades of research and studies by several scientists. A few mentionable are, T. Turbadar from 1950s to 1960s, followed by Heinz Raether, E.Kretschmann and A. Ottio from 1960s till 1970s. Plasmonics is basically the transfer of information or a form of communication in nanoscale where the medium is plasmons.

The scattering of light into the surface causing the nanoparticles to excite has a range of applications. They are used in, energy sector which helps in improving the solar cells, medical sectors in visual images and drug delivery systems. The way the nanoparticles behave to the incoming light is of our main interest, the scattering of light, that is, how much light reflects back depends on the type of the particles, they either absorb or scatter the incoming light and the summation of this is called extinction [2].

Nanoplasmonics is the study of the optical occurring in nanoscale region on metal surfaces [4]. The incident light beam causes the excitation of localized surface plasmons causing the noble-metal nanoparticles that are smaller than the wavelength of light in the visible spectrum resulting in strong resonance for light scattering and absorption. During resonance, the light simultaneously energizes causing combined oscillation of the conduction electrons of the metal nanoparticle, this act as a regular dipole. The resonance frequency depends on the shape and size of the particle and on the dielectric environment (which is later demonstrated in the paper). This condition lets us tune the colour to the visible region and into the near-infrared region of the electromagnetic spectrum, alongside keeping the particle as small as 100nm range [5]

One remarkable mention of this phenomenon has marked its part in the history that is coloured glasses with regards to metal nanoparticles dopants. A dopant is a doping agent, a trace impurity element that is inserted into a substance in small amount which change the electrical and/or optical properties of the substance. Modern applications involve dealing with single nanoparticles that means tagging of biomolecules, this improves the light emission from

nanoscale photon sources and biomolecular sensing. These properties determine the fact that metal nanoparticles enable nano-concentration of incident light below the diffraction limit on conduction electrons at the metal surface which is at the interface between a negative and positive permittivity material at their dipolar resonant frequency, and promote scattering cross-section and resonantly enhanced absorption [5].

The **London Centre for Nanotechnology**, widely known as **LCN** has the most fundamental equipment that is needed to study the properties, fabrication and various characteristics of the nanoparticles. Few mentionable are; high resolution **Transmission Electron Microscopy** (TEM), shows us the properties of plasmonic modes in complex nano structures; **Electron Beam Lithography** also known as **Focused Ion Beam Milling** is needed to produce metallic structures with properties in the visible range; and high resolution Scanning Electron Microscope (SEM) is requires to make sure that the samples that are to be investigates has the desired dimensions and morphology [5].

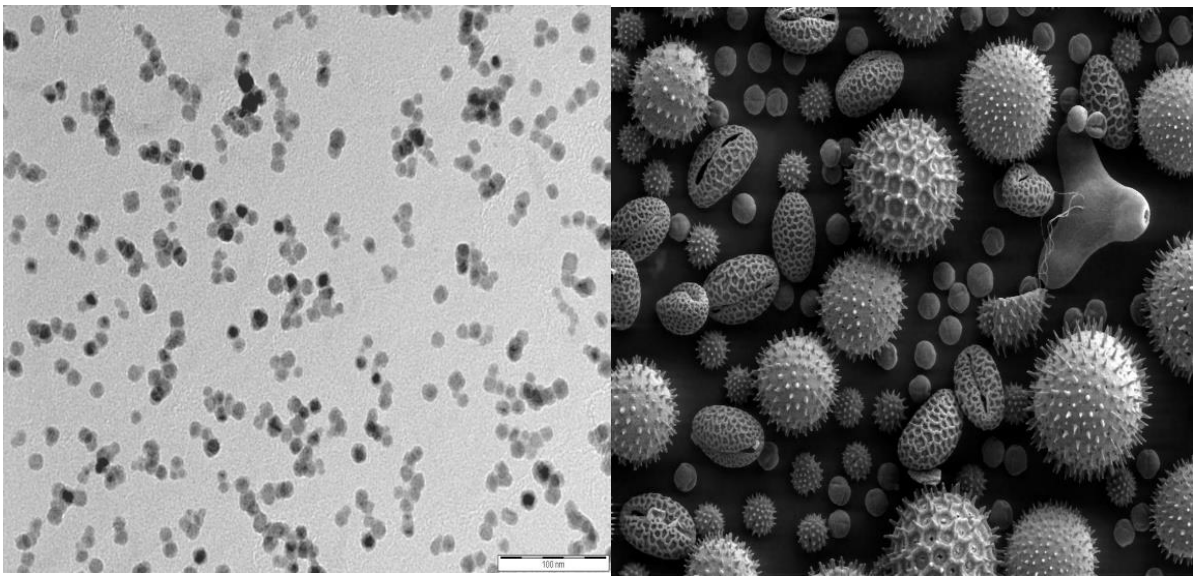

Figure 1.1 *(a) Images of Silver (Ag) nanoparticles obtained from Transmission Electron Microscopy (TEM),* [18], *(b) Images obtained from Scanning Electron Microscope (SEM),* [19]

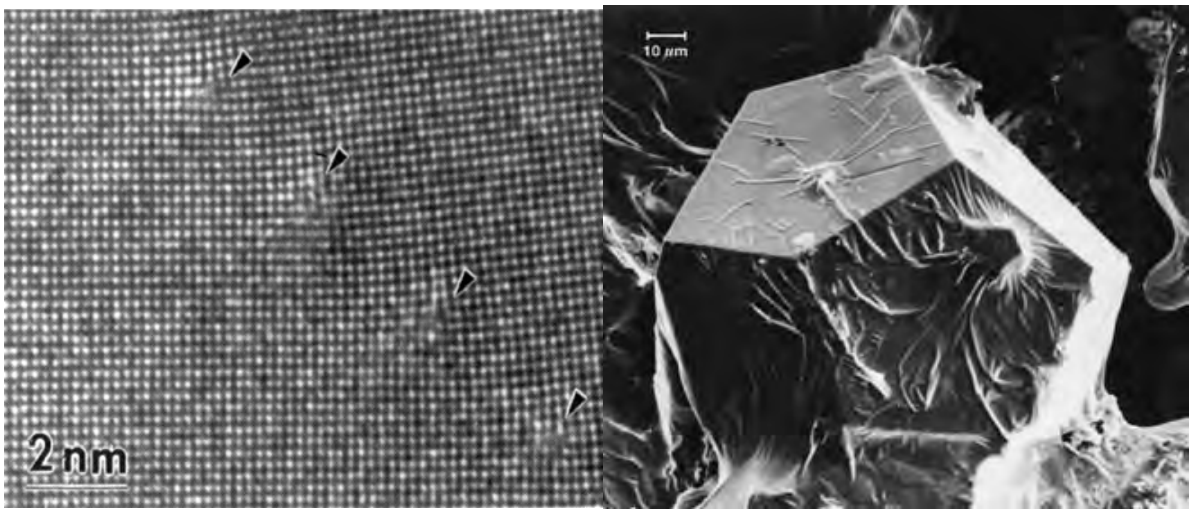

Figure 1.1 *(a) Images of Aluminium (Al) nanoparticles obtained from Transmission Electron Microscopy (TEM),* [70], *(b) Images obtained from Scanning Electron Microscope (SEM),* [71]

1.2 Surface Plasmon Resonance in the Medical Sector

Given the plasmonic connection between metal nanoparticles with the refractive list and the partition are extremely sensitive, surface plasmon resonance is widely used in medical, biological and chemical sensing and recognition applications. The nanoparticles are sensitive to unique sorts of biomolecule and also to the change of dielectric environment causing resonance shift which helps to determine the proof and presence of various chemicals. For this, a thin metal layer, or a surface containing a thick layer of nanoparticle is arranged. These nanoparticles can be made sensitive to molecules. When the substance to be researched is spread over the desired surface particular type of nanoparticles will bring huge change for Localized Surface Plasmon Resonance. Beside this, nanoparticles can be infused into cells again bringing visible changes [6].

Plasmonic interaction between metal nanoparticles depends on their separations, so precise result and measurements of the plasmon resonance wavelength of metal particles can be used as a scale for molecules to operate at a length much larger than that, in terms of fluorescence energy

transfer metrology used in biology. This concept is used practically in systems biology, for example, imaging the motion of the molecule mechanics or structural changes in protein due to external chemicals and in DNA [6].

Other example of a challenging application of this is the use of particles composed of a dielectric core and a metallic shell in cancer treatment. These particles are injected into the human body suspected to have cancer; they then bound to the harmful or mutated molecules selectively, which is one property of them as well. After the formation of the bonding, laser sterilization as a precise engineered plasmon resonance wavelength is projected to heat the particles, which then finally destroys the malicious cells [6].

1.3 Overview of the thesis

Chapter 1

Introduction to Nanoplasmonics and its various uses in optics, photovoltaics and medical sector.

Chapter 2

This chapter overviews the Surface Plasmon Resonance (SPR), Localized Surface Plasmon Resonance (LSPR), the difference and advantages of LSPR over SPR and finally introduces Fano Resonance.

Chapter 3

This chapter discusses our proposed structure, and introduces proteins in the human body as biomolecules and talks about their functionalities.

Chapter 4

Introduction to the software Lumerical and a detailed outline of how it is used in the research is in this chapter.

Chapter 5

This part is all about the research and analysis and the simulation processes being used along with a few drawbacks. Graphs of power absorption, Fano resonance shifts on changing of conditions and factors are explained with detail explanations.

Chapter 6

Finally, this chapter is the conclusion of our thesis paper. We have talked about the arrangement of the nano particle as well we discussed the limitations of our study

2. Physics of Fano Resonance Localized Surface Plasmon Resonance

2.1 Surface Plasmons (SP)

Surface Plasmons are coherent delocalized electron oscillations that exist at the interface between any two materials where the real part of the dielectric function changes sign across the interface (e.g. a metal-dielectric interface, such as a metal sheet in air). The wave created at the interface is called the Evanescent Wave.

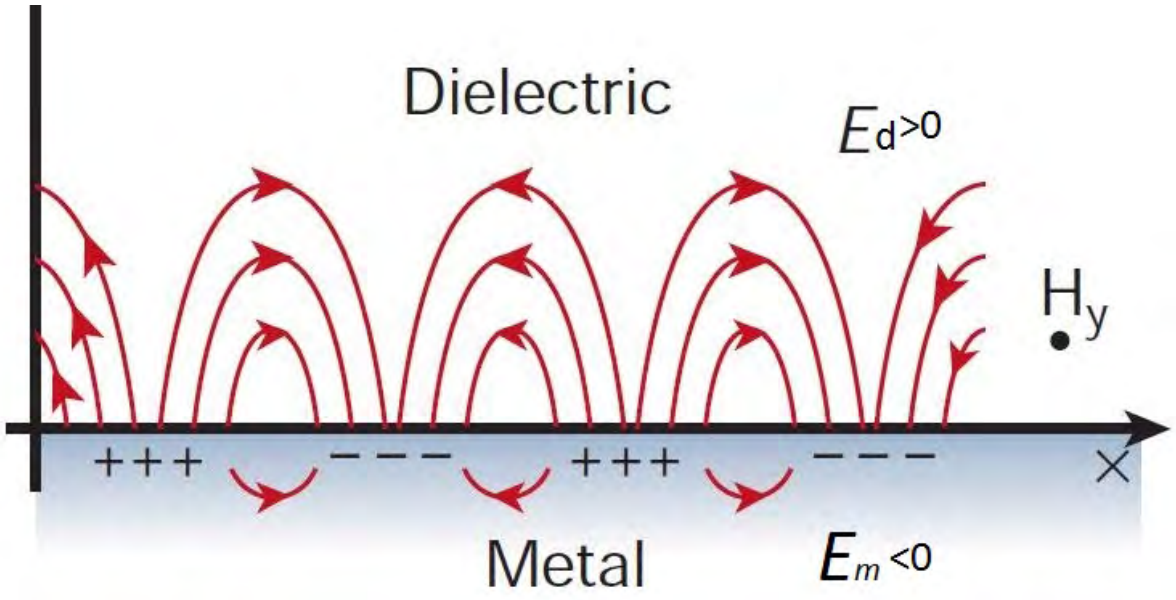

Figure 2.1*Surface Plasmon*

Ed = Permittivity of the dielectric

Em = Permittivity of the metal

2.2 Evanescent Waves

An evanescent wave is a near field wave with an intensity that exhibits exponential decay without absorption as a function of distance from the boundary at which the wave was formed. This means that the energy is confined in a small area in that wave.

There is decay on both sides of the interface and the wave only propagates in the longitudinal direction.

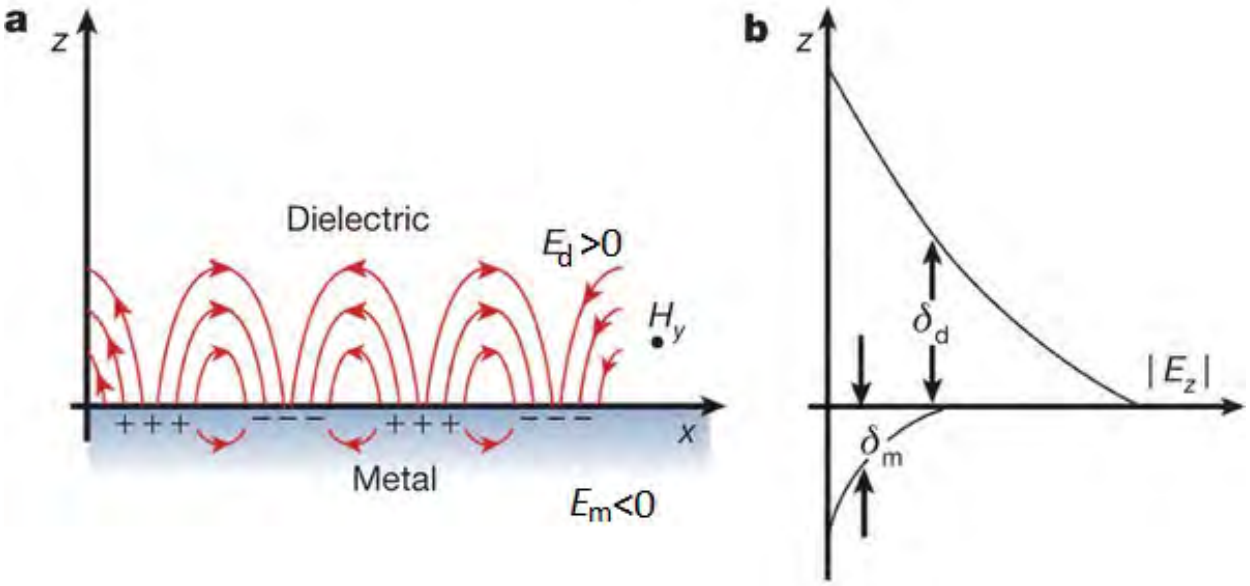

Figure 2.2*Evanescent Wave*

Surface plasmons have brought down vitality than mass (or volume) plasmons which quantize the longitudinal electron motions about positive particle centers inside the main part of an electron cloud or plasma. The charge movement in a SP makes electromagnetic fields both inside and outside the metal. The aggregate excitation, i.e. the charge movement and the related electromagnetic field, is known as a surface plasmon (or surface plasmon polariton, SPP) at a planar interface, or a limited surface plasmon for a little molecule.

2.3 Surface Plasmon Resonance (SPR)

Surface plasmon resonance (**SPR**) is the **resonant** oscillation of conduction electrons at the interface between a negative (Em<0) and positive (Ed>0) permittivity material (metal/air or metal/water) stimulated by incident light. The resonance condition is established when the frequency of incident photons matches the natural frequency of surface electrons oscillating against the restoring force of positive nuclei. SPR in subwavelength scale nanostructures can be polaritonic or plasmonic in nature [7].

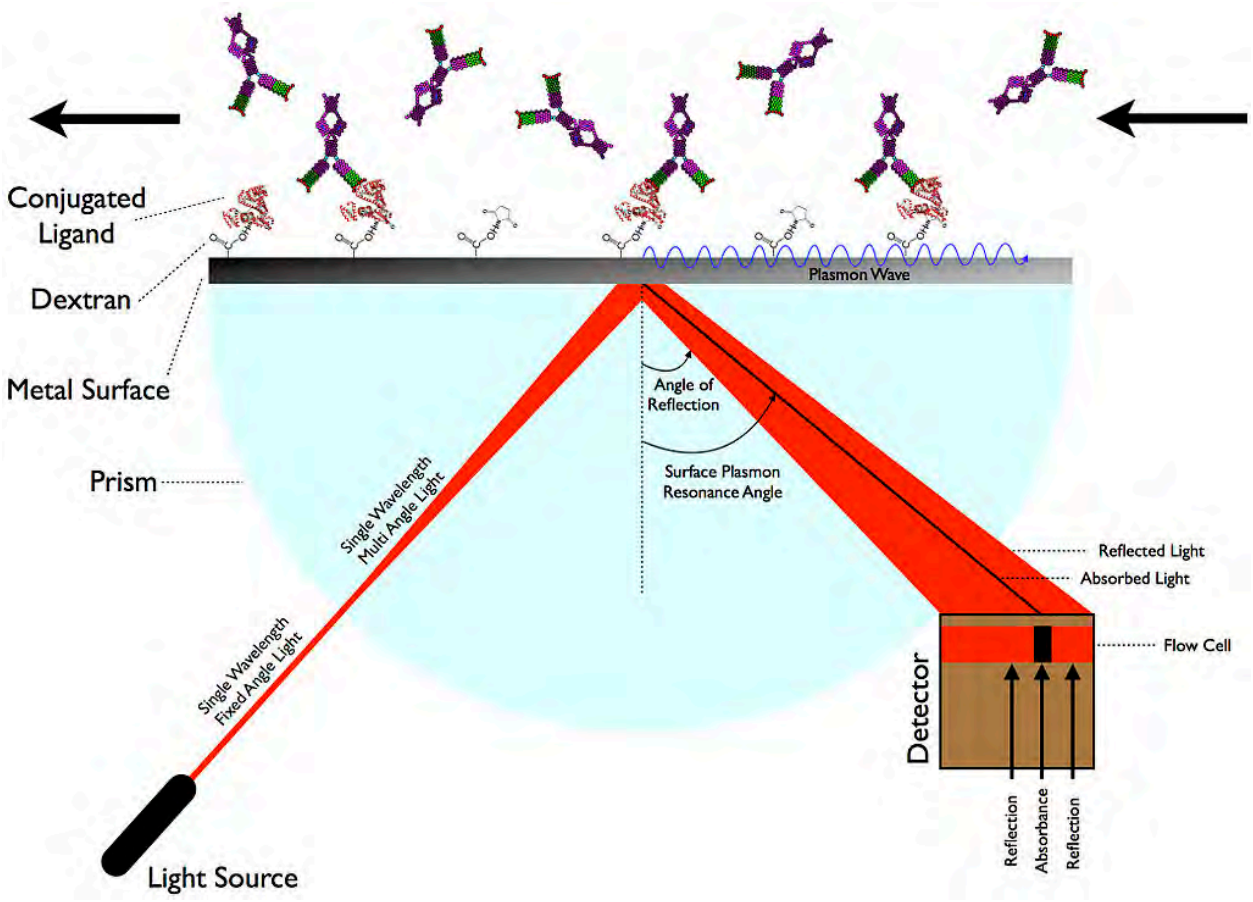

Surface **Figure 2.3***Surface Plasmon Resonance*[7]

SPR is used as the standard tool for measuring adsorption in gold or silver and other nanoparticles [8]. Many colour based sensors work on the theory of SPR. When a single wavelength of fixed angle light is emitted on the surface of a nano-particle the light beam becomes a multi angle light at the moment of hitting the surface. The refracted light beam is

observed and the amount absorbed is noted by the receiver. SPR is a no radiative electromagnetic wave that propagates in the direction of the negative permittivity/dielectric of the material. The wave propagates in the boundary of the conductor and external medium, so a slight change in the boundary condition effects the wave propagation, such as the adsorption. For SPR to occur the real dielectric constant of the conductor but be negative and the magnitude must negative then the dielectric (air/water) and this condition has to be met in visible-infrared wavelength region. Surface plasmons does not penetrate deep in the metal but can propagate several microns away from the surface in the dielectric.

In contrary to conventional wave guides, filed on both sides are always evanescent.

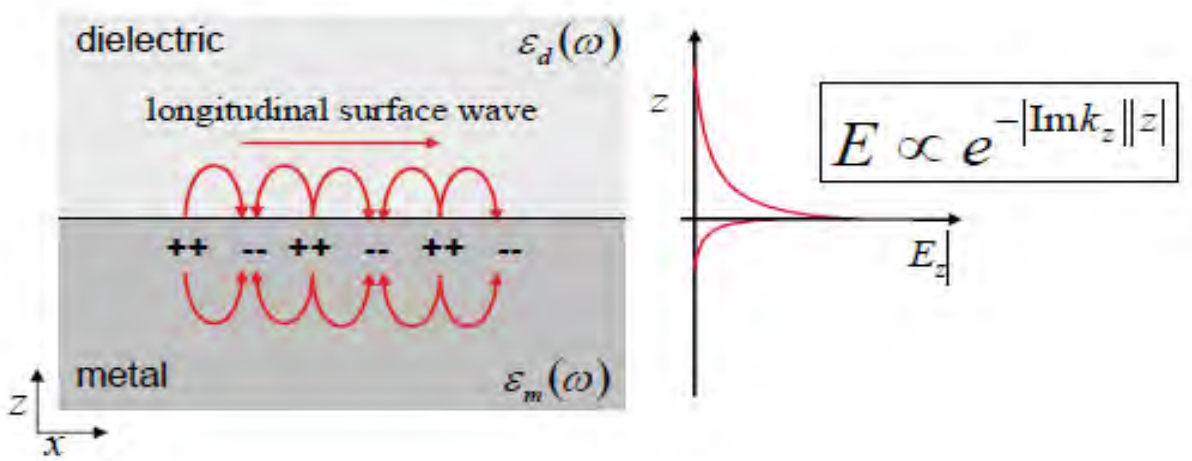

Figure 2.4*Schematic of Surface Plasmon Resonance*[8]

2.4 Localized Surface Plasmon Resonance (LSPR)

Localized surface plasmon (LSP) is the result of the confinement of a surface plasmon in a nanoparticle of size comparable to or smaller than the wavelength of light used to excite the plasmon.

The LSP has two important effects:

1. Electric fields near the particle's surface are greatly enhanced and the particle's optical absorption has a maximum at the plasmonresonant frequency. The enhancement falls off quickly with distance from the surface and, for noble metal nanoparticles, the resonance occurs at visible wavelengths.

2. For semiconductor nanoparticles, the maximum optical absorption is often in the near-infrared and mid-infrared region. The optical absorption of the particle is maximum at the plasmon resonant frequency

Localized Surface Plasmons are non-spreading excitations of the conduction electrons of metallic nanostructures coupled to the electromagnetic field. These modes produce normally from the dispersing issue of a little, sub-wavelength conductive nanoparticle in a wavering electromagnetic field. An agent reestablishing power is applied on the determined electrons by the bended surface of the nanoparticle. Accordingly, a resonance emerges, prompting field enhancement on both inside and in the close field zone outside the molecule. This resonance is called **localized surface plasmon resonance**. Another hugeness of the bended surface is that the plasmon resonances can be created by direct light enlightenment [5].

The thinnest layer of bio-molecule is absorbed at the interface causing a slight but noticeable change in resonance for gold and silver. LSPR senses only a few nanometers into the dielectric and the resonant frequency is easy to measure, even with naked eyes, it is used in nano-scale sensing application and enhanced in modern analytic application in spectroscopy.

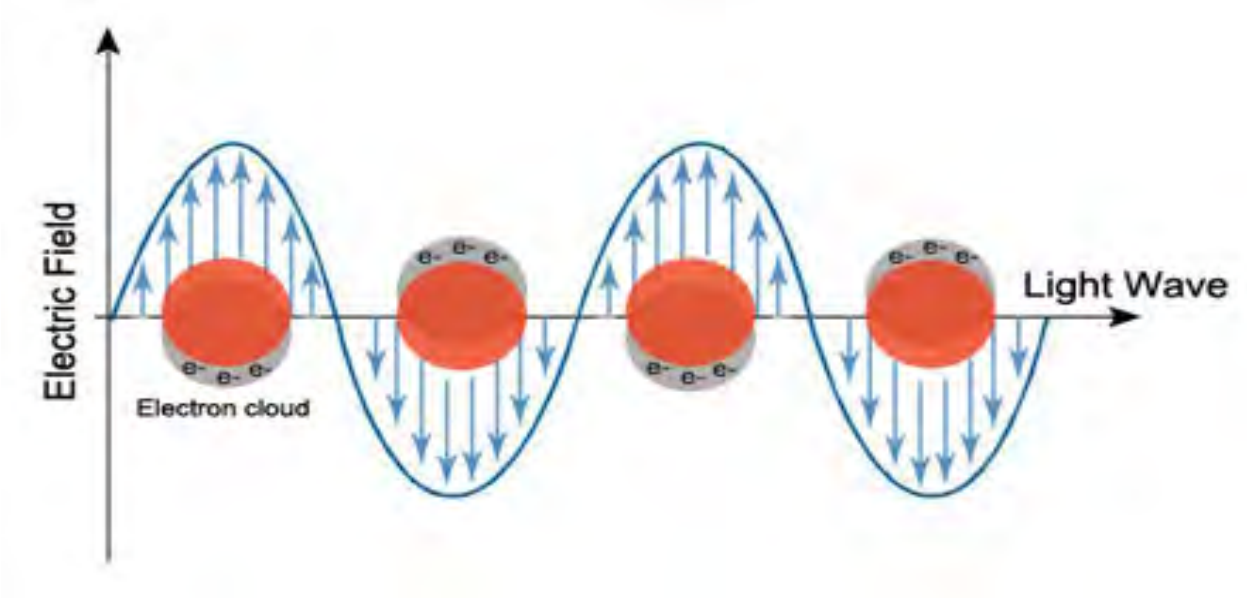

Figure 2.5 *Schematic of Localized Surface Plasmon oscillation of a sphere, showing the displacement of the conduction electron charge cloud relative to the nuclei.* [2]

2.5LSPR on a Metal Nano particle

The interaction of a particle of size *d* with the electromagnetic field can be analyzed by using the **Quasi-Static** approximation, given that $d<<\lambda$, that is, the particle is far smaller than the wavelength of the incident light surrounding the medium. In a case like this, the phase of the harmonically oscillating electromagnetic field is virtually constant over the particle volume. Hence, it is possible to calculate the spatial field distribution by assuming the simplified problem of a particle in an electrostatic field. Once the field distributions are acknowledged, the harmonic time dependence can then be added to the solution. This lowest-order estimation of the full scattering problem describes the optical properties of nanoparticles of proportions below 100 nm, effectively for many purposes [5].

We start with the simplest geometry for an analytical treatment: a homogeneous, isotropic sphere of radius *a*, positioned at the origin in a uniform, static electric field, $\mathbf{E} = E0\ \hat{}\mathbf{z}$. the surrounding medium is isotropic and non-absorbing with dielectric constant *Em*, and the field lines are parallel to the z-direction at an adequate amount of distance from the sphere. The dielectric response of the sphere is further described by the dielectric function $\varepsilon\ (\omega)$, which we consider as a simple complex number ε for the time being [5].

Approaching from an electrostatic point of view, we are concerned in a solution of the **Laplace equation** for the potential, $\nabla 2\Phi = 0$, from which we will be able to calculate the electric field, $\mathbf{E} = -\nabla\Phi$. Due to the azimuthal symmetry of the problem, the general solution is of the form:

$$\Phi(r,\theta) = \sum_{l=0}^{\infty} \left[A_l r^l + B_l r^{-(l+1)}\right] P_l(\cos\theta),$$

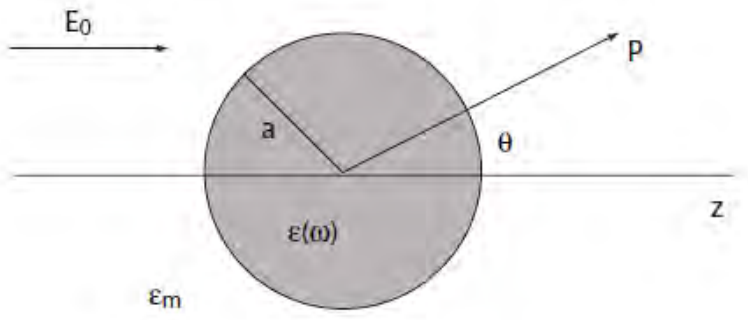

Figure 2.6 *Sketch of a nano particle in an electrostatic field*[5]

where*Pl (*cos *θ)* are the Legendre Polynomials of order *l*, and *θ* the angle between the position vector **r,** at point P and the z-axis. Due to the requirement that the potentials remain finite at the origin, the solution for the potentials Φininside and Φout outside the sphere can be written as:

$$\Phi_{\text{in}}(r,\theta) = \sum_{l=0}^{\infty} A_l r^l P_l(\cos\theta)$$

$$\Phi_{\text{out}}(r,\theta) = \sum_{l=0}^{\infty} \left[B_l r^l + C_l r^{-(l+1)}\right] P_l(\cos\theta).$$

The coefficients *Al, Bl*and *Cl*can now be determined form the boundary conditions at $r \to \infty$ and at the sphere surface $r = a$. The requirement that $\Phi in \to -E0z = -E0r\cos\theta$ as $r \to \infty$ demands that $Bl = -E0$ and $Bl = 0$ for $l \neq 1$. The remaining coefficients *Al* and *Cl* are defined by the boundary conditions at $r = a$. equality of the tangential components of the electric field demands that

$$-\frac{1}{a}\frac{\partial \Phi_{\text{in}}}{\partial \theta}\bigg|_{r=a} = -\frac{1}{a}\frac{\partial \Phi_{\text{out}}}{\partial \theta}\bigg|_{r=a},$$

And the equality of the normal components of the displacement field

$$-\varepsilon_0 \varepsilon \frac{\partial \Phi_{\text{in}}}{\partial r}\bigg|_{r=a} = -\varepsilon_0 \varepsilon_{\text{m}} \frac{\partial \Phi_{\text{out}}}{\partial r}\bigg|_{r=a}.$$

Application of these boundary conditions leads to $Al = Cl = 0$ for $l \neq 1$, and via the calculation of the remaining coefficients *Al* and *Cl*, the potentials evaluate to:

$$\Phi_{\text{in}} = -\frac{3\varepsilon_m}{\varepsilon + 2\varepsilon_m} E_0 r \cos\theta$$

$$\Phi_{\text{out}} = -E_0 r \cos\theta + \frac{\varepsilon - \varepsilon_m}{\varepsilon + 2\varepsilon_m} E_0 a^3 \frac{\cos\theta}{r^2}.$$

It is interesting to interpret the w=equation physically: Φout describes the superposition for the applied field and that of a dipole located at the particle center. We can rewrite Φout by introducing the dipole moment **p** as:

$$\Phi_{\text{out}} = -E_0 r \cos\theta + \frac{\mathbf{p} \cdot \mathbf{r}}{4\pi\varepsilon_0\varepsilon_m r^3}$$

$$\mathbf{p} = 4\pi\varepsilon_0\varepsilon_m a^3 \frac{\varepsilon - \varepsilon_m}{\varepsilon + 2\varepsilon_m} \mathbf{E}_0.$$

Therefore, we see that the applied field introduces a dipole moment inside the sphere of magnitude proportional to |**E**0|. If we introduce the polarizability *a*:

$$\alpha = 4\pi a^3 \frac{\varepsilon - \varepsilon_m}{\varepsilon + 2\varepsilon_m}.$$

This equation is the central result of this section, the complex polarizability of a small sphere of sub-wavelength diameter in the electrostatic approximation. We note that it shows the same functional form as the Clausius-Mossotti relation.

The following figure (Fig. 2.7) shows the absolute value and phase of *a* with respect to frequency *ω* (in energy units) for a dielectric constant varying as *ε(ω)* of the Drude form, in this case fitted to the dielectric response of silver [Johnson and Christy, 1972]. It is obvious that the polarizability experiences a resonant improvement under the condition that |*ε* + 2*εm*| is a minimum, which for the case of small or slowly varying Im[*ε*] around the resonance simplifies to:

$$\text{Re}\left[\varepsilon\left(\omega\right)\right] = -2\varepsilon_m.$$

This relationship is called the Fröhlich condition and the associated mode (in an oscillating field) the *dipole surface plasmon* of the metal nanoparticle. For a sphere consisting of a Drude metal with a dielectric function located in air, the Fröhlich criterion is met at the frequency $\omega 0=\omega p/\sqrt{3}$, which further expresses the strong dependence of the resonance frequency on the dielectric environment: The resonance red shifts as $\varepsilon m$is increased. Metal nanoparticles are thus the ideal platforms for optical sensing of change in refractive index.

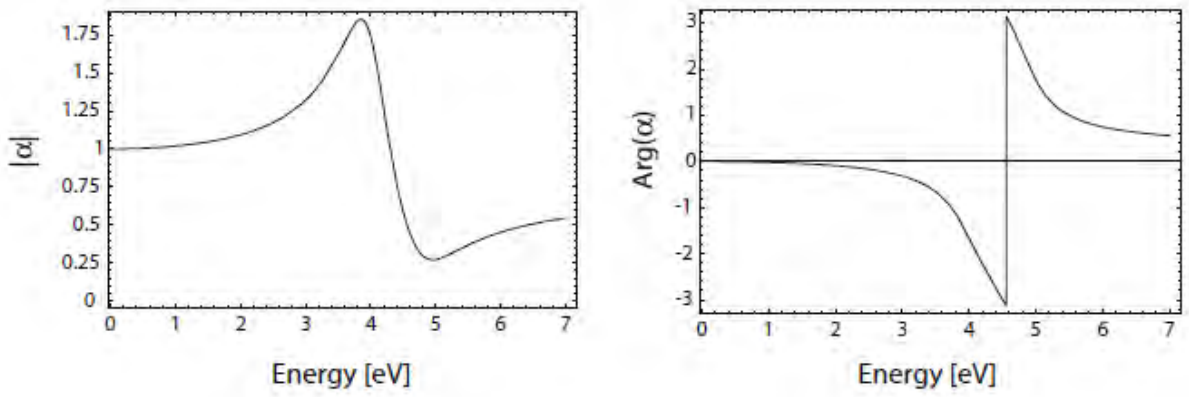

Figure 2.7 *Absolute value and field polarizability α of a sub-wavelength metal nanoparticle with respect to frequency of the driving field (expressed as eV units). Here, ε(ω) is taken as a Drude fit to the dielectric function of silver [Johnson and Christy. 1972].* [5]

We note that the magnitude of α at resonance is limited by the incomplete vanishing of its denominator, due to $\mathrm{Im}[\varepsilon(\omega)] \neq 0$.
The distributions of the electric field $\mathbf{E} = -\nabla\Phi$ can be evaluated from the potentials to:

$$\mathbf{E_{in}} = \frac{3\varepsilon_m}{\varepsilon + 2\varepsilon_m}\mathbf{E}_0$$

$$\mathbf{E_{out}} = \mathbf{E}_0 + \frac{3\mathbf{n}\,(\mathbf{n}\cdot\mathbf{p}) - \mathbf{p}}{4\pi\,\varepsilon_0\varepsilon_m}\frac{1}{r^3}.$$

The resonance in α also implies a resonant enhancement of both the internal and dipolar fields. It is this field enhancement at the plasmon resonance on which many of the prominent applications of metal nanoparticles in optical devices and sensors rely.

We have been on the firm ground of electrostatics, which we will now leave and turn our attention to the electromagnetic fields radiated by a small particle excited at its plasmon resonance. For a small sphere $a << \lambda$, its representation as an ideal dipole is valid in the Quasi-Static regime, i.e. it allows for time-varying fields but neglects spatial retardation effects over the particle volume. Under plane-wave illumination with $\mathbf{E}(\mathbf{r}, t) = \mathbf{E}0e^{-i\omega t}$, the fields introduce an oscillating dipole moment $\mathbf{p}(t) = \varepsilon 0 \varepsilon m \alpha \mathbf{E}0e^{-i\omega t}$, with α given by the electrostatic result. The radiation of this dipole leads to *scattering* of the plane wave by the sphere, which can be represented as radiation by a point dipole.

It is useful to briefly review the basics of the electromagnetic fields associated with an oscillating electric dipole. The total fields $\mathbf{H}(t) = \mathbf{H}e^{-i\omega t}$and $\mathbf{E}(t) = \mathbf{E}e^{-i\omega t}$in the near immediate zones of a dipole can be written as:

$$\mathbf{H} = \frac{ck^2}{4\pi} (\mathbf{n} \times \mathbf{p}) \frac{e^{ikr}}{r} \left(1 - \frac{1}{ikr}\right)$$

$$\mathbf{E} = \frac{1}{4\pi \varepsilon_0 \varepsilon_m} \left\{ k^2 (\mathbf{n} \times \mathbf{p}) \times \mathbf{n} \frac{e^{ikr}}{r} + [3\mathbf{n} (\mathbf{n} \cdot \mathbf{p}) - \mathbf{p}] \left(\frac{1}{r^3} - \frac{ik}{r^2}\right) e^{ikr} \right\},$$

With $k = 2\pi/\lambda$ and $\mathbf{n}$ the unit vector in the direction of the point P of interest. In the near zone $(kr << 1)$, the electrostatic result for the electric field is recovered;

$$\mathbf{E} = \frac{3\mathbf{n} (\mathbf{n} \cdot \mathbf{p}) - \mathbf{p}}{4\pi \varepsilon_0 \varepsilon_m} \frac{1}{r^3}$$

And the accompanying magnetic field present for oscillating fields amounts to:

$$\mathbf{H} = \frac{i\omega}{4\pi} (\mathbf{n} \times \mathbf{p}) \frac{1}{r^2}.$$

We can see that within the near field, the fields are predominantly electric in nature, since the magnitude of the magnetic field is about a factor $\sqrt{(\varepsilon 0/\mu 0)}$ (kr) smaller than that of the electric field. For static fields $(kr \rightarrow 0)$, the magnetic field vanishes.

In the opposite limit of the radiation zone, defined by $kr >> 1$, the dipole fields are of the well-known spherical-wave form:

$$\mathbf{H} = \frac{ck^2}{4\pi}(\mathbf{n}\times\mathbf{p})\frac{e^{ikr}}{r}$$
$$\mathbf{E} = \sqrt{\frac{\mu_0}{\varepsilon_0\varepsilon_m}}\mathbf{H}\times\mathbf{n}.$$

We will now leave this short summary of the properties of dipolar radiation. It is much more interesting from the view point of optics to note that another consequence of the resonantly enhanced polarization α is a concomitant enhancement in the efficiency with which a metal nanoparticle scatters and absorbs light. The corresponding cross sections for scattering and absorption *Csca*and *C*abs can be calculated via the Poynting-vector determined from above [Bohren and Huffman, 1983] to:

$$C_{\text{sca}} = \frac{k^4}{6\pi}|\alpha|^2 = \frac{8\pi}{3}k^4a^6\left|\frac{\varepsilon-\varepsilon_m}{\varepsilon+2\varepsilon_m}\right|^2$$
$$C_{\text{abs}} = k\,\text{Im}\,[\alpha] = 4\pi ka^3\,\text{Im}\left[\frac{\varepsilon-\varepsilon_m}{\varepsilon+2\varepsilon_m}\right].$$

For small particles with $a << \lambda$, the efficiency of absorption scaling with *a3*, dominates over the scattering efficiency, which scales with *a6*. We point out that no explicit assumptions were made in our derivations so far that the sphere is indeed metallic. The expressions for the cross sections are thus valid also for the dielectric scatterers, and demonstrate a very important problem for practical purposes. Due to rapid scaling of *C*sca∝*a*6, it is very difficult to pick out small objects from a background of larger scatterers. Imaging of nanoparticles with dimensions below 40 nm, are immersed in an background of light scatterers can thus usually only be achieved using photo-thermal techniques relying on the slower scaling of the absorption cross section with size. Equations also show that indeed for metal nanoparticles, both absorption and scattering (and thus extinction) are resonantly enhanced at the dipole particle plasmon resonance, i.e. when Frölich condition is met. For a sphere of volume *V* and dielectric function $\varepsilon = \varepsilon 1 + i\varepsilon 2$ in the Quais-Statc limit, the explicit expression for the extinction cross section *C*ext = *C*abs + *C*sca is:

$$C_{\text{ext}} = 9\frac{\omega}{c}\varepsilon_m^{3/2}V\frac{\varepsilon_2}{[\varepsilon_1+2\varepsilon_m]^2+\varepsilon_2^2}.$$

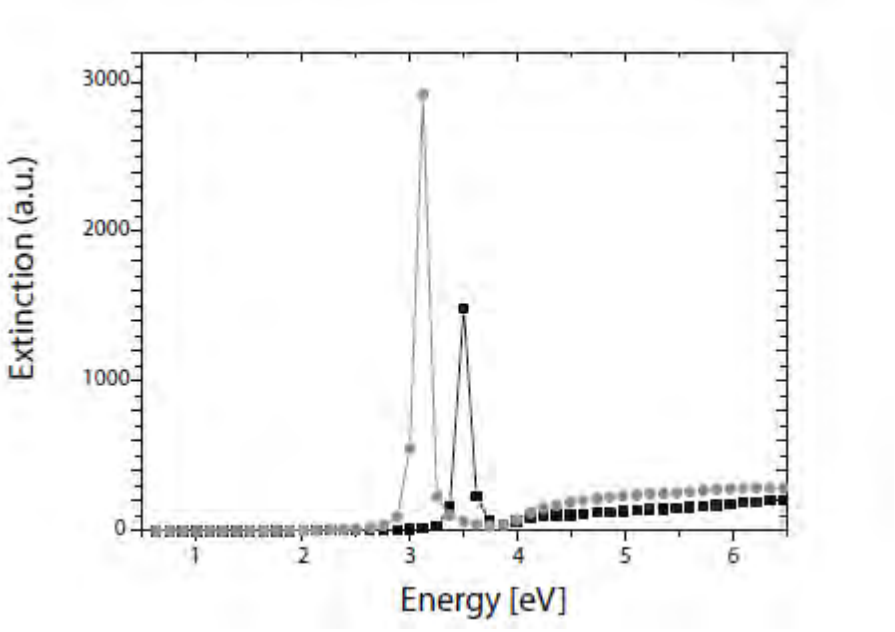

Figure 2.8 *Extinction cross section for a sliver sphere in air (black curve) and in silica (grey curve), with the dielectric data taken from [Johnson and Christy, 1972]* [5]

The above figure shows the extinction cross section of a sliver sphere in the Quasi-Static approximation calculated using this formula for immersion in two different media. In this paper we are working with a rod which is a closed end cylinder that has the same radius all over. It can be considered as a sphere which has been elongated through the middle towards one axis [5].

2.6 Difference between SPR and LSPR

Localized Surface Plasmon Resonance is produced by metal nanoparticles on the surface of the metal, typically gold and silver (silver and aluminium according to this paper), on the other hand Surface Plasmon Resonance requires a continuous film of metal, especially gold.

Conventional SPR is very much similar to open SPR and gives similar results and information under the same conditions and systems. Open SPR is what conventionally known as Localized surface plasmon resonance, but to anybody everything between other SPR instruments and Open SPR will appear the same.

On the contrary LSPR produces a sharp resonance peak and is also visible to the naked eyes, using the conventions of Fano Resonance; its position is extremely sensitive to the nearby

refractive index of the molecule. This way, LSPR measures every little change in the wavelength from the absorbance position, in place of the angles in the conventional SPR [9].

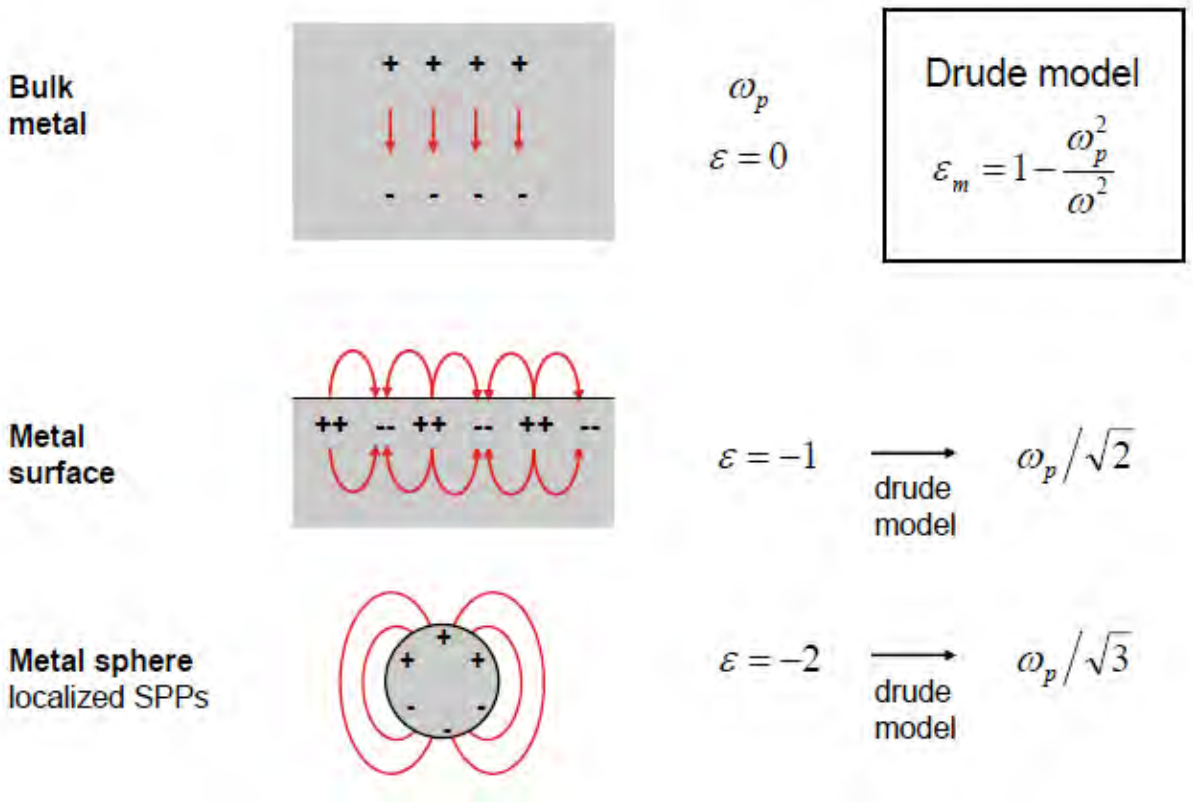

Figure 2.9 *Plasmon Resonance positions in vacuum*[8]

Advantages of LSPR over SPR:

1. The optical instruments required for LSPR is a lot less perplexing since no prism is used to couple the light. This makes the instrument smaller and affordable.

2. Since the edge is not fundamental, the instrument is impressively heartier against vibration and mechanical commotion

3. LSPR id less sensitive to bulk refractive index changes since it has shorter electromagnetic field decay length; this gives more precise information and a better curve.

4. The instrument is not temperature sensative, making the instrument more straightforward to utilize

5. The sensor chips can be made at a more sensible cost

6. Easier to utilize and maintain

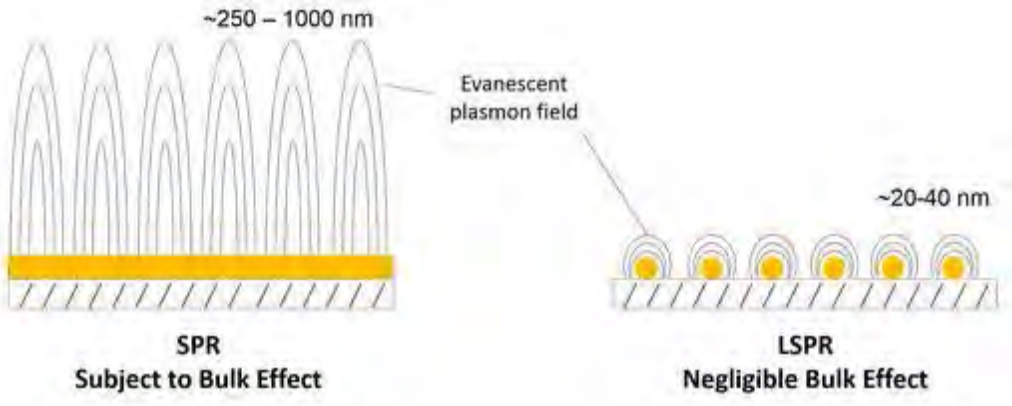

Figure 2.10 *Difference between SPR and LSPR showing bulk effect*[9]

2.7 Fano resonance:

The Fano resonance line-shape is due to interference between two scattering amplitudes, one due to scattering within a continuum of states (the background process) and the second due to an excitation of a discrete state (the resonant process). The energy of the resonant state must lie in the energy range of the continuum (background) states for the effect to occur. Near the resonant energy, the background scattering amplitude typically varies slowly with energy while the resonant scattering amplitude changes both in magnitude and phase quickly. It is this variation that creates the asymmetric profile.

A Fano resonance can appear in Mie theory for light scatteringfrom a single spherical plasmonic particle. In Mie theory, theextinction, scattering and absorption cross-sections are given byexpressions of the form $\sigma = \pi a 2Q$, where a is the radius of the particleand Q the corresponding efficiency. The scattering efficiency isdefined by:

$$Q_{\text{sca}} = \frac{2}{q^2} \sum_{\lambda=1}^{\infty} (2\lambda + 1) \left\{ |a_\lambda|^2 + |b_\lambda|^2 \right\}$$

Where, a_λ and b_λ are electric and magnetic amplitudes, respectively,which depend on the size parameter $q = \omega a/c$ (c is the speed oflight in a vacuum and ω the incident-light frequency and also on the dielectric permittivity ε and the magnetic permeability μ. Thescattering amplitudes are defined by the Mie formulas:

$$a_\lambda = \frac{\mathfrak{R}_\lambda^{(a)}}{\mathfrak{R}_\lambda^{(a)} + i\mathfrak{I}_\lambda^{(a)}}, \; b_\lambda = \frac{\mathfrak{R}_\lambda^{(b)}}{\mathfrak{R}_\lambda^{(b)} + i\mathfrak{I}_\lambda^{(b)}}$$

The Fano resonance line-shape is due to interference between two scattering amplitudes, one due to scattering within a continuum of states (the background process) and the second due to an excitation of a discrete state (the resonant process).The energy of the resonant state must lie in the energy range of the continuum (background) states for the effect to occur. Near the resonant energy, the background scattering amplitude typically varies slowly with energy while the resonant scattering amplitude changes both in magnitude and phase quickly. It is this variation that creates the asymmetric profile.

Fano resonance in Plasmonic nanostructure:

The Fano resonance in plasmonic nanostructure can be derived from the Maxwell's equation

There are three coupling regime in Fano resonance; in the weak coupling regime a high sensitivity of radioactive opening channel is observed for the dark mode, the highest electromagnet field enchantment is observed in the optimal regime when the in and out coupling balance intrinsic loss and feature of Fano resonance is altered for stronger coupling regime.

The basic concept for fano resonance is intervention between the overlapping broad and wide resonance of spectra's. It is possible to create tunable coupled plasmonic structures which are made by conventional plasmonic materials like gold or silver to satisfy conditions for fano resonance. It is not necessary that the structure of the particle have to be the spherical shaped, changing the geometry and spacing between the particle's structures can independently control the width and energies of plasmon resonance [66].

2.8 Summary

Surface plasmon resonance is the resonant oscillation of conduction electrons at the interface between negative ($\varepsilon m < 0$) and positive ($\varepsilon d > 0$) permittivity material stimulated by incident light. Upon incidence of light whose frequency matches with that of the natural frequency of the conduction electrons, the oscillation of the conduction electrons in the metal and dielectric interface generates a propagating evanescent wave. The electric field propagates both inside and outside the metal. The generation of evanescent waves proves that the energy is confined in a small area where the light has hit the metal surface.

A Localized Surface Plasmon Resonance (LSPR) is the result of the confinement of a surface plasmon in a nanoparticle of size comparable or smaller than the wavelength of the light in the visible range or the light used to excite the plasmon. Unlike Surface Plasmons, Localized Surface Plasmons are **non-propagating** excitations of the conduction electrons of metallic nanostructures coupled to the electromagnetic field. These modes naturally generate an oscillating electromagnetic field from the scattering problem of a small, sub-wavelength conductive nanoparticle. As a result, a resonance arises, leading to field amplification on both inside and in the near-field zone outside the particle. This resonance is called **localized surface plasmon resonance**.

The advantages of LSPR over SPR include:

- ✓ High molecular sensitivity
- ✓ Simplicity of instrumentation
- ✓ Cost effectiveness

For aluminiumand silver nanoparticles, the resonance falls into the visible range of the electromagnetic spectrum. It is solely because of this that the bright colors are displayed by particles both in transmitted and reflected light, due to resonantly improved absorption and scattering. This application has made itself very useful for many centuries, for example, in the staining of glass in windows or ornamental cups.

The line and shape of the Fano Resonance is due to interference between two scattering amplitudes, one due to scattering within a continuum of states and the second due to an excitation of a discrete state. The energy of the resonant state must lie in the energy range of the continuum (background) states for the effect to occur. Near the resonant energy, the background scattering amplitude typically varies slowly with energy while the resonant scattering amplitude changes both in magnitude and phase quickly. It is this variation that creates the asymmetric profile.

3. Bimetallic Nanorod Tunable Nanoparticles Biosensor:

3.1 Analyzed Structure

The proposed structure of the thesis is the arrangement of two metal nanorods, Aluminum (Al) and Silver (Ag) arranged by end-to-end with a small gap in between. Although Fano Resonance is known to have a lesser extent in heterogeneous nanostructure constituted by nanoparticles of different metals both theoretically and experimentally concentrating on Au-Ag heterodimers but this paper presents a theoretical proof of Fano Resonance in a new kind of heterogeneous metallic nanostructure of Al-Ag nanorods. It is found out that Al nanorods exhibit high tunable plasmonic resonance from deep ultraviolet to visible wavelength region. The experimental setup is shown below:

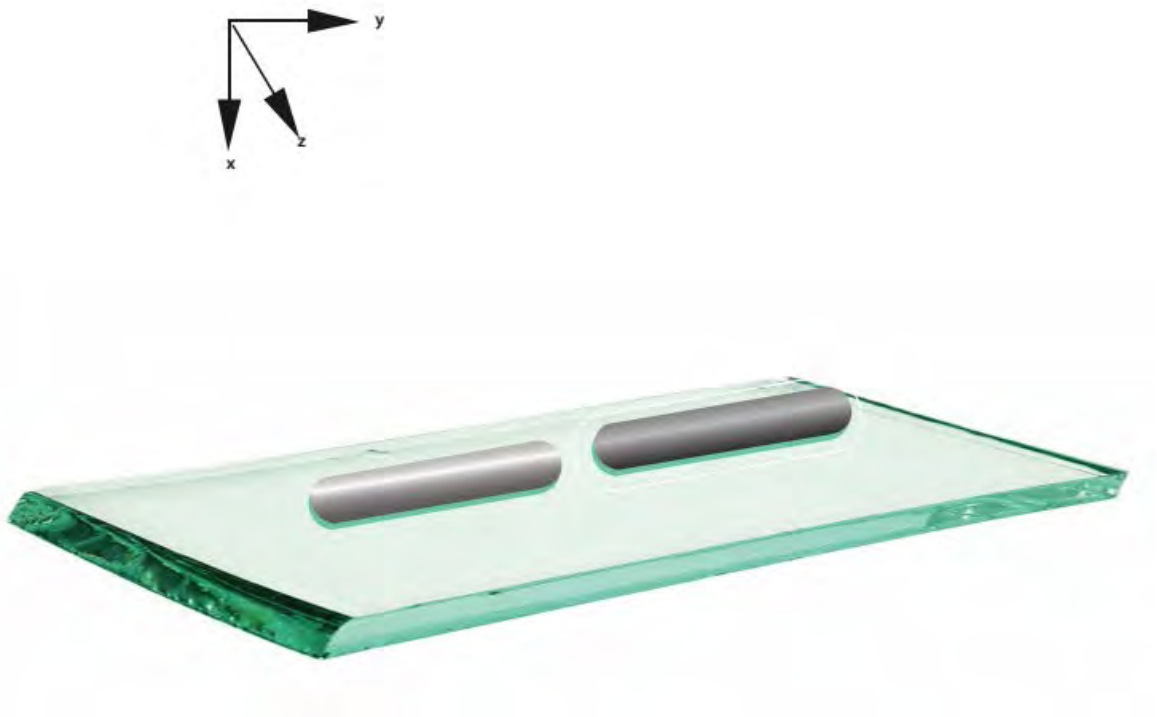

Figure 3.1: *Illustration of Analyzed Structure*

The short nanorod is the Al nanorod which supports a broad bright mode and the longer nanorod is the Ag nanorod that supports a narrow dark mode. The nanorods are placed on top of a substrate of SiO2 (glass). The whole of it is then immersed in water and the entire setup is illuminated with light. Initially the Al rod is 142nm long and the Ag rod is 200nm, both their

diameters are 2R=40nm and the gap between them is d=10nm. The Fano dip can be tuned by changing various aspects of the setup.

First the power absorption curve for the change in d is noted, keeping the length and diameter constant, followed by the change in length of one rod at a time again keeping the d and diameter constant. Then the change in the Fano dip with change in refractive index is noted and calculated and finally with different protein molecules.

The later part of the paper will demonstrate the complete experiment in detail with supporting proofs and curves.

3.2 Protein as a Biomolecule

Any type of molecule which are present in living organisms are said to be biomolecule or biological molecule. Biological molecule can be large molecules or can be small molecules as well. Large molecules are carbohydrates, proteins, starch lipids, nucleic acids and so on. Small molecules are primary metabolites, secondary metabolites and natural products. Main elements of biomolecules are carbon and hydrogen with nitrogen, oxygen, sulphur and phosphorus.

Chemically, protein is composed of amino acids, which are organic compounds made of carbon, hydrogen, nitrogen, oxygen or sulfur. Amino acids are the building blocks of proteins, and proteins are the building blocks of muscle mass, according to the National Institutes of Health (NIH) [11].

The biomolecules or proteins are used for the thesis is given below:

- **Lysozyme (Lys)**
  Refractive Index
  1. 80ug/mL TiO_2 – 1.475
  2. 40ug/mL TiO_2 – 1.495
  3. 6M Urea – 1.48
  4. 40 Teflon – 1.51

- **Human Serum Albumin (HAS)**
  Refractive Index
  1. 80ug/mL TiO_2 – 1.415
  2. 40ug/mL TiO_2 – 1.445
  3. 6M Urea – 1.41
  4. 40 Teflon – 1.435

- **Human Immunoglobulin G (IgG)**
  Refractive Index
  1. 80ug/mL TiO_2 – 1.415
  2. 40ug/mL TiO_2 – 1.48
  3. 6M Urea – 1.42
  4. 40 Teflon – 1.38

- **Fibrinogen (Fb)**
  Refractive Index
  1. 80ug/mL TiO_2 – 1.405
  2. 40ug/mL TiO_2 – 1.40
  3. 6M Urea – 1.43
  4. 40 Teflon – 1.38

3.2.1 Lysozyme (Lys)

In the early twentieth century lysozyme was discovered by Alexander Fleming. Lysozyme is a special type of enzyme which can be found in salvia, sweat, breast milk, tears and other type of body fluids. It is also found in egg white. It mainly works as antibacterial enzyme. Lysozyme is capable of destroying the growth of bacteria. Carbohydrate and Peptidoglycan layer are the elements which are present in the cell walls of bacteria and lysozyme breaks down the elements, in this way it can stop the growth of bacteria. It catalyzes the hydrolysis of 1,4-β linkages between N-acetylmuramic acid and N-acetyl-D-glucosamine.

The enzyme functions by attacking peptidoglycans (found in the cell walls of bacteria, especially Gram-positive bacteria) and hydrolyzing the glycosidic bond that connects *N*-acetylmuramic acid with the fourth carbon atom of N-acetylglucosamine. It does this by binding to the peptidoglycan molecule in the binding site within the prominent cleft between its two domains. This causes the substrate molecule to adopt a strained conformation similar to that of the transition state. According to Phillips-Mechanism, the lysozyme binds to a hexasaccharide. The lysozyme then distorts the fourth sugar in hexasaccharide (the D ring) into a half-chair conformation. In this stressed state, the glycosidic bond is easily broken [12].

Lysozymes plays different role in different type of cancers. Cancer cells can create lysozyme in such a huge amount that high concentration of lysozyme can be found on blood stream. The increased amount of lysozyme in blood causes kidney disorder or kidney failure. It also decreases the amount of potassium and electrolyte levels in blood. If doctors remove the malignant tumor then this situation can be improved [12].

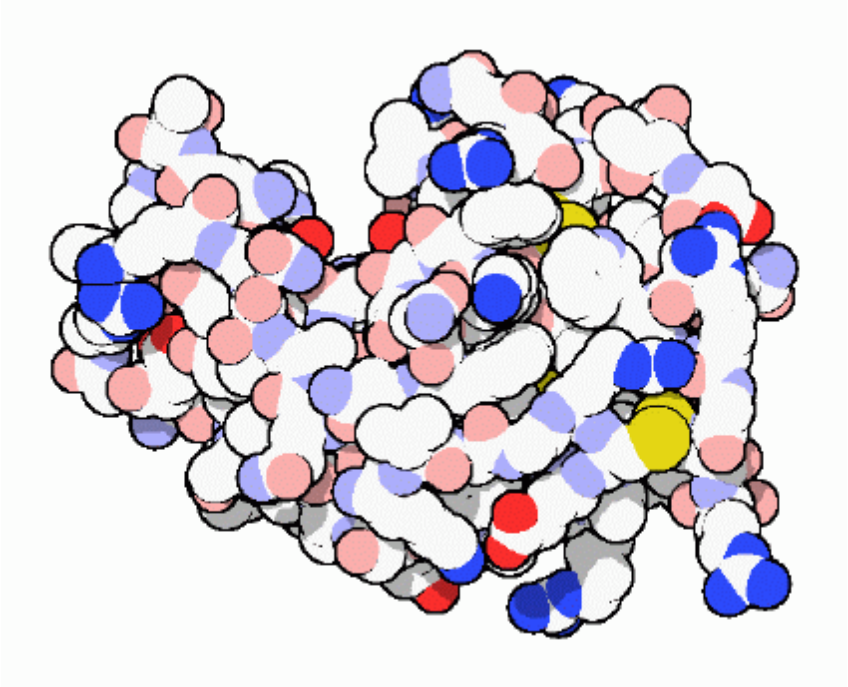

Figure 3.2 *Lysozyme* [16]

3.2.2 Human Serum Albumin (HSA)

Serum albumin present in human blood is said to be the human serum albumin. This serum is soluble, monomeric and produced in liver. It is a globular protein of 585 amino acids. The amount of HSA in blood is the almost 60% of the total protein present in blood serum.

Albumin is synthesized in the liver as preproalbumin which has an N-terminal peptide that is removed before the nascent protein is released from the rough endoplasmic reticulum. The product, proalbumin, is in turn cleaved in the Golgi vesicles to produce the secreted albumin. Albumin is a soluble, monomeric protein which comprises about one-half of the blood serum

protein. Albumin functions primarily as a carrier protein for steroids, fatty acids, and thyroid hormones and plays a role in stabilizing extracellular fluid volume. Mutations in this gene on chromosome 4 result in various anomalous proteins. Albumin is a globular unglycosylated serum protein of molecular weight 65,000. The human albumin gene is 16,961 nucleotides long from the putative 'cap' site to the first poly (A) addition site. It is split into 15 exons which are symmetrically placed within the 3 domains that are thought to have arisen by triplication of a single primordial domain. HSA is widely used to stabilize blood volume generally from donors but the fear of contamination such as HIV & Hepatitis has enticed great interest in the recombinant form which is identical to the natural blood. Suitable for use in biochemical, excipient (an inert substance used as a diluent or vehicle for a drug), culture media and chromatographic applications. [13]

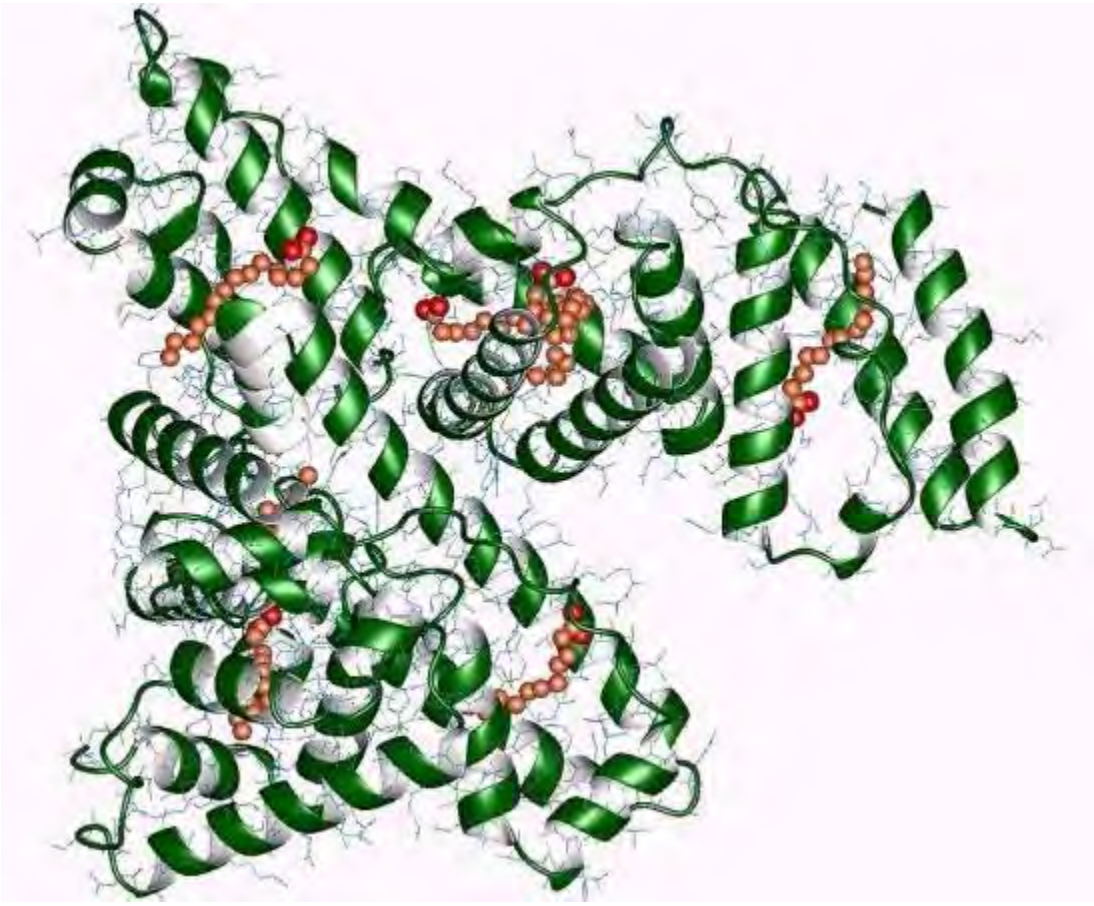

Figure 3.3 *Human Serum Albumin* [13]

3.2.3 Human γ-immunoglobulin (IgG)

Immunoglobulin G (IgG) is a type of antibody. It is a protein complex composed of four peptide chains: two identical heavy chains and two identical light chains arranged in a Y-shape typical of antibody monomers. Each immunoglobulin G molecule has two antigen binding sites. IgG is the most common type of antibody found in the circulation and is responsible for approximately 75% of serum antibodies in humans. IgG molecules are created and released by plasma B cells.

Antibodies are major components of humoral immunity. IgG is the main type of antibody found in blood and extracellular fluid. This causes it to control infection of body tissues. By binding many kinds of pathogens such as viruses, bacteria, and fungi, IgG protects the body from infection.

It does this through several mechanisms:

- IgG-mediated binding of pathogens causes their immobilization and binding together via agglutination; IgG coating of pathogen surfaces (known as opsonization) allows their recognition and ingestion by phagocytic immune cells leading to the elimination of the pathogen itself;
- IgG activates the classical pathway of the complement system, a cascade of immune protein production that results in pathogen elimination;
- IgG also binds and neutralizes toxins;
- IgG also plays an important role in antibody-dependent cell-mediated cytotoxicity (ADCC) and intracellular antibody-mediated proteolysis, in which it binds to TRIM21 (the receptor with greatest affinity to IgG in humans) in order to direct marked virions to the proteasome in the cytosol.;[2]
- IgG is also associated with type II and type III hypersensitivity reactions.

IgG antibodies are generated following class switching and maturation of the antibody response and thus participate primarily in the secondary immune response. IgG is secreted as a monomer that is small in size allowing it to easily penetrate tissues. It provides protection to the fetus in the utero since it is the only isotope that has receptors to create passages through the human placenta. Along with Immunoglobulin A (IgA) secreted in the breast milk, residual IgG absorbed through the placenta provides the neonate with humoral immunity before its own immune system develops. Colostrum contains a high percentage of IgG, especially bovine colostrum. In individuals with prior immunity to a pathogen, IgG appears about 24–48 hours after antigenic stimulation.

Hence, in the first six months of life, the fetus has the same antibodies as the mother, till the old antibodies are then degraded and he can defend himself against all the pathogens that the mother came across in her life (even if only through vaccination). This selection of immunoglobulin is crucial for the newborns that are very sensitive to infections above all for the respiratory and digestive systems.

It is also confirmed that in adults, the production of IgG is linked to the nutritional dominance of a specific food or food-group in the personal diet. As a result, the levels of IgG for food reflect dietary intake or express a possible previous immune contact with food. The total IgG values towards specific foods indicate excessive or repetitive consumption of them. IgG are also involved in the regulation of allergic reactions. According to Finkelman, there are two pathways of systemic anaphylaxis: antigens can cause systemic anaphylaxis in mice through classic pathway by cross-linking Immunoglobulin E (IgE) bound the mast cell FcεRI, stimulating histamine and PAF release. In the Alternative pathway antigens form complexes with IgG that cross-link macrophage Fc γ RIII, stimulating only PAF release.

IgG antibodies can prevent IgE mediated anaphylaxis by interrupting a specific antigen before it binds to mast cell associated with IgE. Consequently, IgG antibodies block systemic anaphylaxis induced by small quantities of antigen but can intercede systemic anaphylaxis induced by larger quantities [14].

Figure 3.4 *Human Immunoglobulin G* [17]

3.2.4: Fibrinogen (Fb)

Fibrinogen (*factor I*) is a glycoprotein in vertebrates that helps in the formation of blood clots. It consists of a linear array of three nodules held together by a very thin thread which is estimated to have a diameter between 8 and 15 Angstrom (Å). The two end nodules are alike but the center one is slightly smaller. Measurements of shadow lengths indicate that nodule diameters are in the range 50 to 70 Å. The length of the dried molecule is 475 ± 25 Å.

The fibrinogen molecule is a soluble, large, and complex 340 kDa plasma glycoprotein, that is converted by thrombin into fibrin during blood clot formation. It has a rod-like shape with dimensions of 9 × 47.5 × 6 nm and it shows a negative net charge at physiological pH (IP at pH 5.2). Fibrinogen is synthesized in the liver by the hepatocytes. The concentration of fibrinogen in the blood plasma is 200–400 mg/dL (normally measured using the Clauss method).

During normal blood coagulation, a coagulation cascade activates the zymogen prothrombin by converting it into the serine protease thrombin. Thrombin then converts the soluble fibrinogen into insoluble fibrin strands. These strands are then cross-linked by factor XIII to form a blood clot. FXIIIa stabilizes fibrin further by incorporation of the fibrinolysis inhibitors alpha-2-antiplasmin and TAFI (thrombin activatable fibrinolysis inhibitor, procarboxypeptidase B), and binding to several adhesive proteins of various cells. Both the activation of factor XIII by thrombin and plasminogen activator (t-PA) are catalyzed by fibrin. Fibrin specifically binds the activated coagulation factors factor Xa and thrombin and entraps them in the network of fibers, thus functioning as a temporary inhibitor of these enzymes, which stay active and can be released during fibrinolysis. Research from 2011 has shown that fibrin plays a key role in the inflammatory response and development of rheumatoid arthritis.[67]

The usefulness of fibrinogen as a marker of inflammation, trauma and various types of infections have been reported in a number of scientific papers

- **General inflammatory response due to an infection:** Fibrinogen normally increases within 24 to 48 hours from a normal level of 2-4 g/L and may exceed 10 g/l on day 4 - 7 post infection. It is not uncommon in horses to have increased plasma fibrinogen levels as the sole indicator of inflammation.
- **Surgical trauma:** Levels of serum amyloid A, fibrinogen and iron reflect the intensity of the surgical trauma, whereas WBC do not do this. Fibrinogen is therefore a good diagnostic marker to monitor the healing process after a surgical procedure.
- **Bacterial infection:** The fibrinogen level can be used to predict the time course of an bacterial infection as has been shown with Escherichia coli endotoxin. It has also been shown to be an effective screening tool to diagnose RhodococcusEqui infections in foals. Fibrinogen concentrations has also been shown to enable a more precise diagnosis of the

severity of an inflammation than that based simply on clinical conditions in respiratory diseases, particularly bacterial pneumonia.

- **Viral infection:** Horses with equine influenza and herpes virus 2 has been proven to show elevated fibrinogen levels 3 days post infection.
- **Parasite infection:** Parasitized (Strongelus Vulgaris) ponies showed in a study to have significantly elevated fibrinogen levels compared to a control group 9, 14, 21 and 45 days after infection. *Heidmann*
- **Aseptic arthritis:** Experimentally induced aseptically inflammation showed a significant increase in fibrinogen with a maximum level 3 - 6 days post-injections. [68]

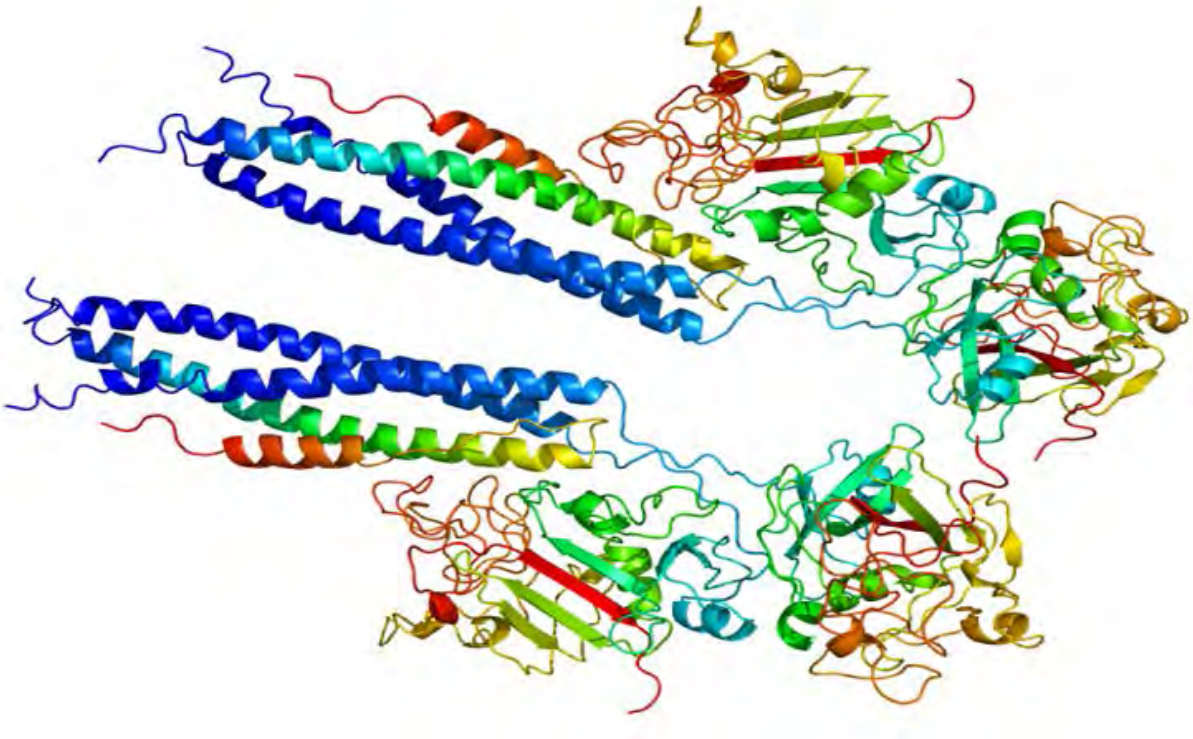

Figure 3.5 *Fibrinogen* [69]

3.3 Summary

Any type of molecule which are present in living organisms are said to be biomolecule or biological molecule. Main elements of biomolecules are carbon and hydrogen with nitrogen, oxygen, sulphur and phosphorus. These biomolecules has a universal name which is biological material. In the sector of biology and biochemistry, biomolecules and their reactions are considered for research and analysis. These molecules are consists of hydrogen, carbon, nitrogen, oxygen and sulfur.

.Lysozyme is a special type of enzyme which can be found in salvia, sweat, breast milk, tears and other type of body fluids. It is also found in egg white. It mainly works as antibacterial enzyme. Lysozyme is capable of destroying the growth of bacteria. Carbohydrate and Peptidoglycan layer are the elements which are present in the cell walls of bacteria and lysozyme breaks down the elements, in this way it can stop the growth of bacteria. It catalyzes the hydrolysis of 1,4-β linkages between N-acetylmuramic acid and N-acetyl-D-glucosamine.

Serum albumin present in human blood is said to be the human serum albumin. This serum is soluble, monomeric and produced in liver. It is a globular protein of 585 amino acids. The amount of HSA in blood is the almost 60% of the total protein present in blood serum. Albumin is synthesized in the liver as preproalbumin which has an N-terminal peptide that is removed before the nascent protein is released from the rough endoplasmic reticulum.

Human γ-chain was split by low concentrations of trypsin and the digests were analyzed by SDS-PAS gel electrophoresis. A number of discrete bands appeared in time with apparent mol. wt of (in thousands) 43, 31, 25, 18, and 12, while the molecular weight of the γ-chain was 56,000 by this method. These values are in agreement with preferential splitting of the γ-chain between, but not inside, the four domains (homology regions), assuming that the carbohydrate side chain on $C_\gamma 2$ contributes an apparent mol. wt increase of about 6000, and independent of the size of the peptide chain to which it is attached.

Fibrinogen (*factor I*) is a glycoprotein in vertebrates that helps in the formation of blood clots. It consists of a linear array of three nodules held together by a very thin thread which is estimated to have a diameter between 8 and 15 Angstrom (Å). The two end nodules are alike but the center one is slightly smaller. Measurements of shadow lengths indicate that nodule diameters are in the range 50 to 70 Å. The length of the dried molecule is 475 ± 25 Å.

4. FDTD Solutions

4.1 Introduction

We are trying to create two metallic Nano rods, one of which is composed of Silver (Ag) and the other is composed of Aluminum (Al). The nanostructure has to be placed on a Silicon Dioxide (SiO_2) substrate, very closely side by side. The whole system has to be enlightened with light. Then we can observe the Power Absorption Curve of the Nano rods. Additionally, we analyze the electric field coupling of destructive interference between a broad super radiant bright mode and a narrow sub-radiant dark mode.

4.1.1. Broad super-radiant bright mode and narrow sub-radiant dark mode

If one system is pumped at frequencies resonant with both bright and dark modes, the bright mode will be excited by two pathways:[***I*** to ***B***]and[***I*** to ***B*** to ***D*** to ***B***] , where ***I*** , ***B*** and ***D*** are sources of excitation , bright mode, and dark mode, respectively. Fano-like interference occurs when the cumulative phase shifts from ***B*** to ***D*** to ***B*** is Pi so that the two pathways interfere destructively, canceling the polarization of the bright mode and resulting in a narrow Fano dip in the extinction spectrum [21] as will be shown in the P_{abs} curve later on.

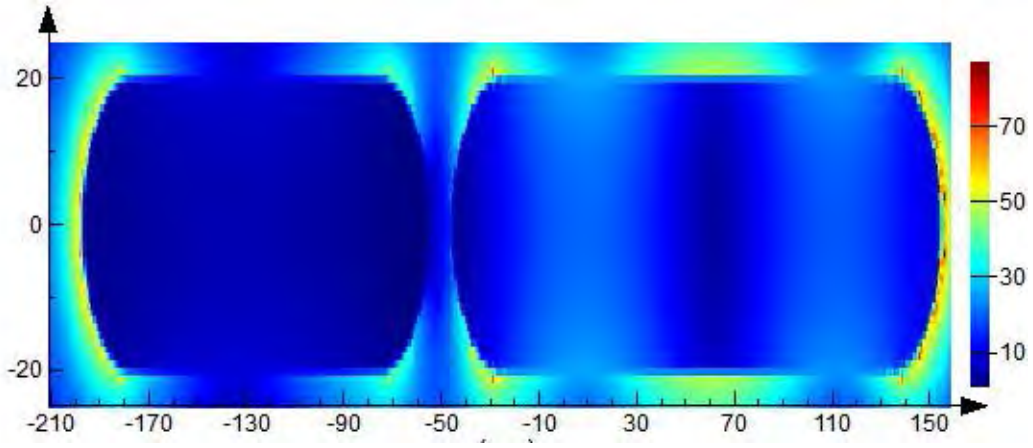

Figure 4.1: *Electric field Distribution across the Central Cross Section at* ***λ****=579 nm*

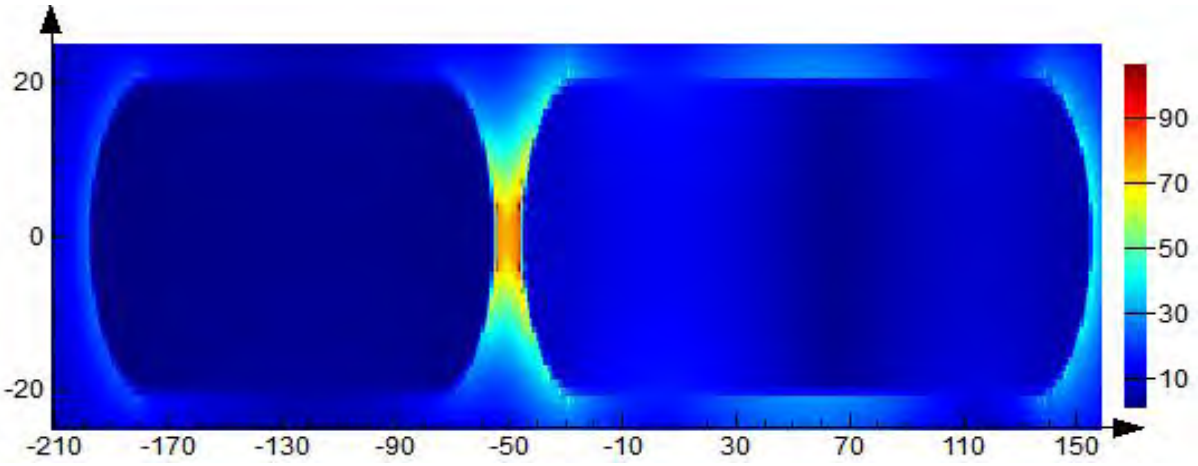

Figure 4.2: *Electric field Distribution across the Central Cross Section at* λ*=621.8 nm*

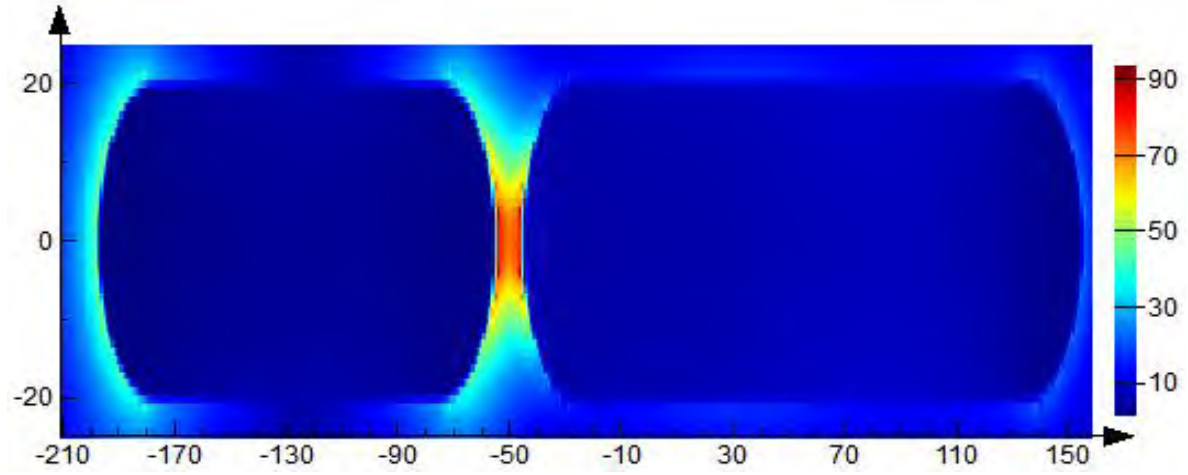

Figure 4.3:*Electric field Distribution across the Central Cross Section at* λ*=686.7 nm*

Simultaneously, the dipole and quadrupole plasmon modes supported by the shorter Al and longer Ag nanorods couple in a constructive way to create two collective resonant modes: a high-energy antibonding mode at 579.1 nm and a low-energy bonding mode at 621.8 nm. The electric field distributions of the dimer with the separation d = 10 nm at the wavelength of 579.1, 621.8 and 686.7 nm are shown in Figures. The electric field enhancement of the dimer at the Fano dip is greatly depressed due to the cancelation of its polarization in the Fano resonance.

4.2 About Lumerical

The name **Lumerical** is a compound word consisting of two words: the fore word '***Luminous'*** meaning full of light, illuminated and '***Numerical'*** meaning of or relating to a number or a series of numbers; as it is advertised in the company's own website. Their tagline being, "Achieve more with light".

Figure 4.4: *Lumerical Logo* [15]

As their name suggests the company develops software that simulates photonic interaction, tools that help the designers to understand light and predict its interaction with structures, circuits and systems. Lumerical's design tools allow scientists to create, test, and optimize their product designs without crafting physical prototypes. These predictive capabilities enable the scientific and engineering community to validate designs prior to manufacturing, create new product concepts, and explore long-term innovative photonics research. The company provides 4 different software for component design, FDTD Solutions, MODE Solutions, DEVICE Charge Transport, DEVICE Heat Transport. Among these we shall only use FDTD Solutions for our purposes.[15]

4.2.1 FDTD Solutions

This software from **Lumerical** is a high performance 3D Finite Difference Time Domain (FDTD) method Maxwell solver for the design, analysis and optimization of Nano photonic devices, processes and materials.[22] It has various applications and key applications include:

- CMOS Image Sensors.
- Solar Cells.
- OLEDs.
- Integrated Optics.
- Surface Metrology.
- Surface Plasmons.
- Metamaterials.
- Photonic Crystals.
- Liquid Crystals.
- Graphene.

4.3 Structure Modeling

At first the software is installed and opened. Four windows appear on the screen, each with a significance of its own. The top left window shows the 'xy' plane, the bottom left window shows the 'xz' plane, the bottom right window shows the 'yz' plane and the top right window displays the 3D ('xyz') illustration of the particle. On the left of it there is a panel for the objects tree that shows the things we have in the system we are trying to build. Above the four windows rest a panel that shows a list of materials, structures, attributes, components, sources, analysis and monitors we can get for the modeling of our system. Last but not least the top right shows a panel to check all the resources and memory requirements to run the simulation and a button to actually run it.

First, we go to the "Settings" and set the length units to nanometers as we are working with nanoparticles and structures here. Now, we have to make the 2 nanorods in their baseline state. The baseline state in our case being the length of the Ag nanorod is 200 nm and the length of the Al nanorod is 142 nm while the gap between them in 10 nm and they both have a radius of 20 nm. We go to Components > Cylindrical > Rounded Cylinder. This structure comes as a structure group which means it is a cylinder with two spheres at each end to make a rod or a rounded cylinder. We have to place two of these rods to simulate the Al and the Ag nanorod.

Next, we have to select the nanorod on top and make it into the desired Ag nanorod. By right clicking on the structure group we access the option to edit that object. In the editing panel of the object we get to look at the script that runs the simulation for that object. We can change its index, material, radius, radius ends, and z span where index means refractive index; radius is the radius for the cylinder and radius ends is the radius for the spheres at the end and lastly z span means the length of the cylinder. Then, we hop on to the properties tab to change all our

variables. Here we want our rods to be long and variable on the y axis. Therefore, the origin points are set (-16.25, 54.8, 0) for (x, y, z) axis. The refractive index is set to 1.4 for Ag and so is the material selected from library as Ag (Silver) – Johnson and Christy. Both radius and radius ends are 20 nm. And the z span (length) is changed to 200 nm for the baseline test.

Following the same procedure for the bottom rod we make the Al nanorod. This one uses the material Al (Aluminium) – CRC and has a length of 142 nm. Both nanorods are named as Ag_cyl and Al_cyl for identification later.

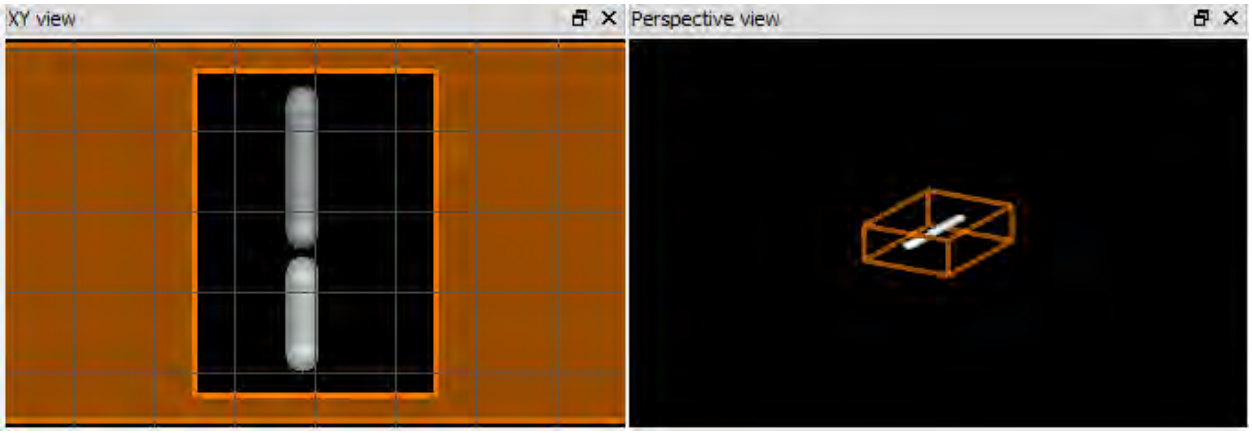

Figure 4.5: *Ag and Al Nanorods*

4.4 Substrate Formation

We have already created our nanorods but we still have to create the substrate that the rods have to be placed on. The substrate can be created from various types of materials. For our simulation we shall be using Glass (SiO_2). SiO_2 is basic sand glass. It is indeed very cheap. Now, in order to apply the substrate to our setup, we take the following directions “Structure > Rectangle”. Then we edit this object according to our necessities; we change the “Geometry” of the rectangle. There are six options: x (nm), y (nm), z (nm), x span (nm), y span (nm) and z span (nm). The values of y and z are set to 0. The values of y and z spans are 600 nm each. The value of x is set to 152.45 nm and the value of x span is set to 295.5 nm. The x, y, z values represent the origin point of the substrate. And the spans represent its width along each axis.

The values of the geometry of the substrate are set with accuracy so that the substrate only touches our nanorods on the positive 'y' side on the 'xy' view. The refractive index of Silicon Dioxide is 1.46 and there are a few advantages of using Silicon Dioxide over other substrates.

Advantages of Silicon Dioxide:

- Outstanding thermal stability.
- Low expense coefficient.
- Compressive stress preload.
- High strength (1 GPa) and stiffness.
- Excellent thickness control.
- Easily reworked die attach.

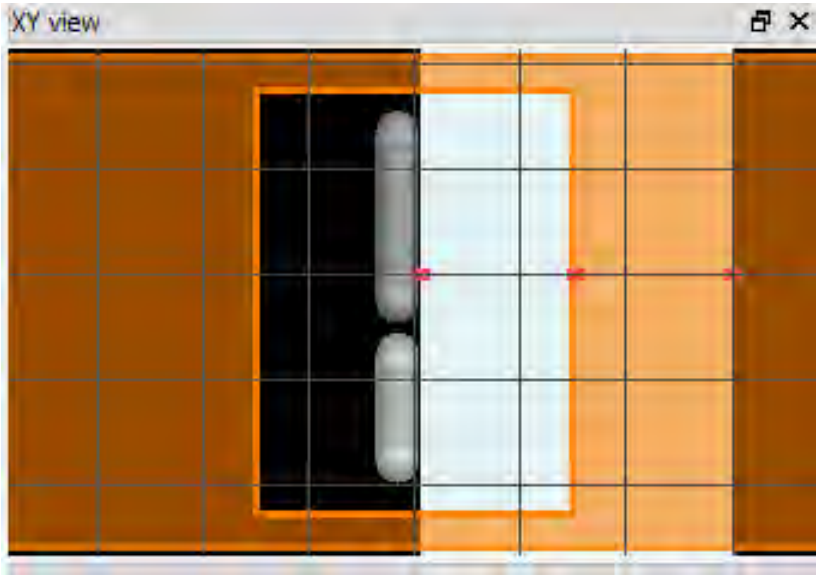

Figure 4.6: *Nanorods with Substrate*

This completes the formation of our basic structure of two closely placed nanorods on a glass substrate surface.

4.5 FDTD – Finite Difference Time Domain

FDTD allows us to change the surroundings of the nanoparticle to create the experimental setup to ensure the proper conditions required for our thesis research. We use this to create the basic water or buffer solution that our structure is within and later in the process this is used to simulate the different samples of biomolecules and their refractive indexes.

4.5.1 General

We go to “Simulation > Region > General”. An option appears named “FDTD”. We edit the object by setting the value of the “background index” to 1.33 to match the refractive index of water or a buffer solution. This ensures that the nanoparticle is completely immersed in water. Then, “Simulation Time” is set to 300 fs. As the simulation time increased to a larger value, the size of the file increases highly and it takes a very long time to obtain he results. On the other hand, if we set the simulation time to too much of a small value, we will not get the desired results. Hence, we have selected an optimum value of 300 fs.

4.5.2 Geometry

Now, we have selected the “Geometry” option located right next to “General”. There are six options: x (nm), y (nm), z (nm), x span (nm), y span (nm) and z span (nm). The values of x and z are set to 0 and y to -26.2 which happens to be the origin point of our structure. This ensures that the simulation will occur over a range and not over a fixed value. That is why we use the x, y, z span options. The value of each span we are setting is 300, 400, 0 nm of x, y and z span respectively. This means that FDTD is automatically taking the nanorod couple as the center and there is a length of approximately 40 nm in ‘y’ direction around the rods.

4.5.3 Boundary Conditions

The boundary conditions that are supported by FDTD/MODE Solutions, which we have used for our research, are listed below. The values of “x min bc”, “x max bc”, “y min bc”, “y max bc”, “z min bc” and “z max bc” have been set to PML. The option “allow symmetry on all boundaries” have been unchecked. In the PML settings the “pml reflection” has been set to 0.0001. The applications and explanations of PML is listed below.

4.5.3.1 Perfectly Matched Layers (PML)

By construction, PML absorbing boundary conditions are impedance matched to the simulation region and its materials. This allows them to absorb light waves (both propagating and evanescent) with minimal reflection. An ideal PML boundary produces zero reflections, however, in practice there will always be small reflections due to the decentralization of the underlying PML equations. Furthermore, as a consequence of using finite difference approximations to decentralize the PML equations, there is some chance of producing numerical instabilities. The goal of this section is to outline best practices for minimizing reflection errors and getting rid of numerical instabilities without increasing simulation times unnecessarily.

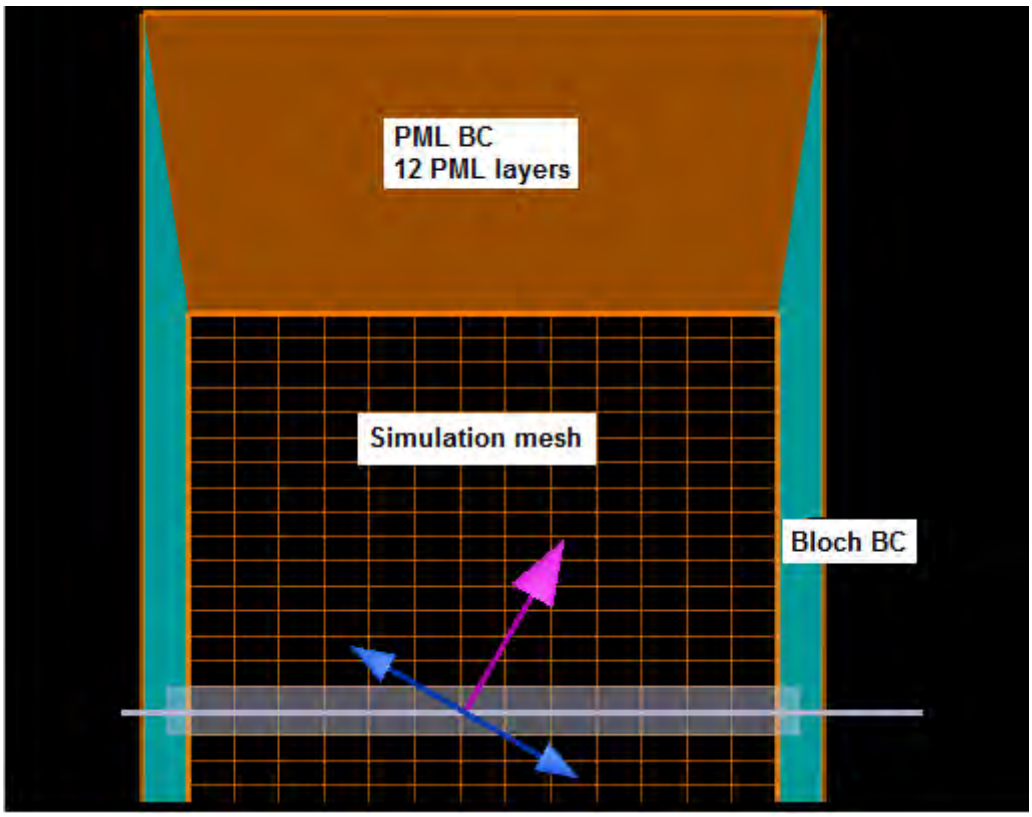

Figure 4.7: *Schematic of PML* [23]

4.6 Mesh Analysis

After setting the conditions in FDTD, we can start with the mesh analysis. Accessibility of mesh is obtained from “Simulation > Mesh”. The values of the “General” settings are set to 1 because lower values guarantee better accuracy. However, we do not take values less than 1, such as 0.5

or 0.25, because this increases the size of the file so much that the simulation time increases highly and after a few minutes into the simulation, the file shows an error and stops as our desktops did not have enough memory to support the computation. We can only use 0.5 of the mesh value to get a smooth and good quality result for electric filed, but not the entire simulation.

In this application, we use a combination of graded meshing and conformal meshing. The conformal meshing allows us to obtain more accurate results for a given mesh size. Even if the mesh size is only twice as large, for example 2 nm compared to 1 nm, the computation time in 3D simulations can be reduced by a factor of 16. We need to be careful when using conformal mesh technology with metals, however, and do some convergence testing to be sure that the conformal mesh technology is appropriate for one's precise application.[24]

Now, we select the mesh and go to its edit object. In the editing panel in "General" we override x, y and z mesh and set dx (nm) to 2. Afterwards, we proceed to the "Geometry" tab. In this tab just like most other geometry edits in this application we can set the origin point for our mesh with the x, y and z options while setting the width of each axis through its respective span. We set the origin point to (-15.25, -26.2, 0). Also the span is set to 50, 370 and 50 for x, y and z respectively. Later we will change the origin and the span to suite the variable lengths of the rods. These values will only be set as the baseline simulation. But in general we try to keep at least 5 nm gap between the rods and the mesh in each direction (x, y, z) around the particle.

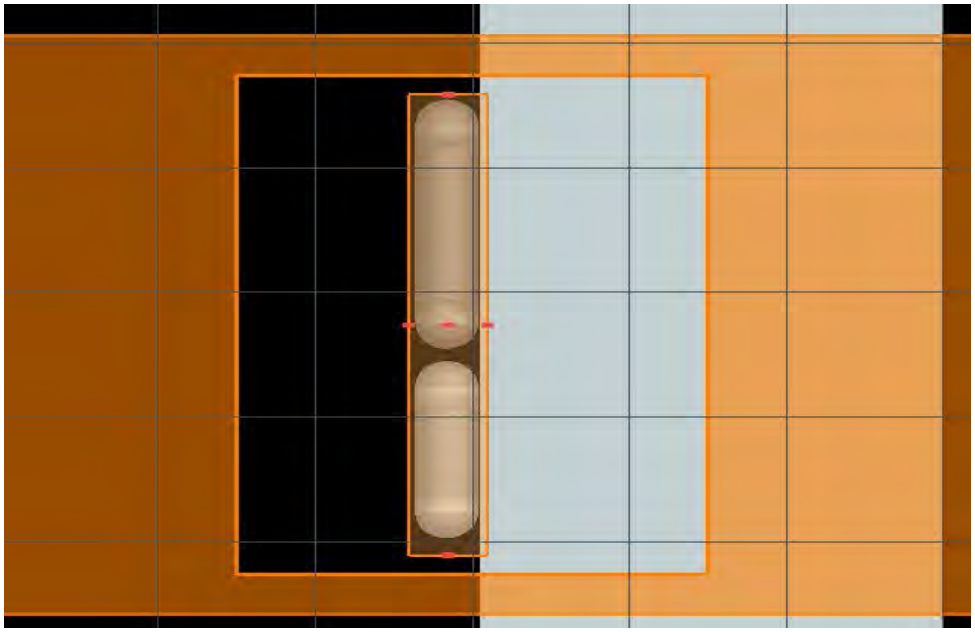

Figure 4.8: *Structure with Mesh Selected*

4.7 Source

This is the light source that is being used to illuminate the entire experimental setup. With the purpose of adding a light source to our already existing apparatus, we follow “Sources > Total Field Scattered Field (TFSF)”. This installs the light source in the setup. Now, the object is edited to fit our testing.

In the “General” tab of the source we have an ‘injection axis’, this determines at which axis the light falls. We set this to the x-axis so it hits the nanorods and then the substrate. The direction is set to forward. Lastly, with all the phase and angles set to 0 we set the amplitude to 5.

We move on the “Geometry” settings for our source. Once again the geometry is set up with origin point (x, y, z) and spans (x span, y span, z span). These settings for the light source are changed with variable lengths of the rods and the space in between them but always set so that they cover the whole structure and the mesh of the simulation.

Lastly we have to deal with the last settings of “Frequency/Wavelength” tab. In this tab we can set either the frequency/wavelength range of the light or the time domain. At first we check the “override global source settings”. Then we check the “set frequency/wavelength” box. This is done because we will be varying the wavelength range to get our results. In the “set frequency/wavelength” box we first choose wavelength and then a range between min and max. Wavelength start (nm) is set to 500 and the wavelength stop (nm) is set to 900. We predict our peaks and dip to be present within this range as we first set in to 200 to 1000 and got the initial graph. But such a long range wastes simulation time when our needed peaks and dips are situated in the 500 to 900 nm region.

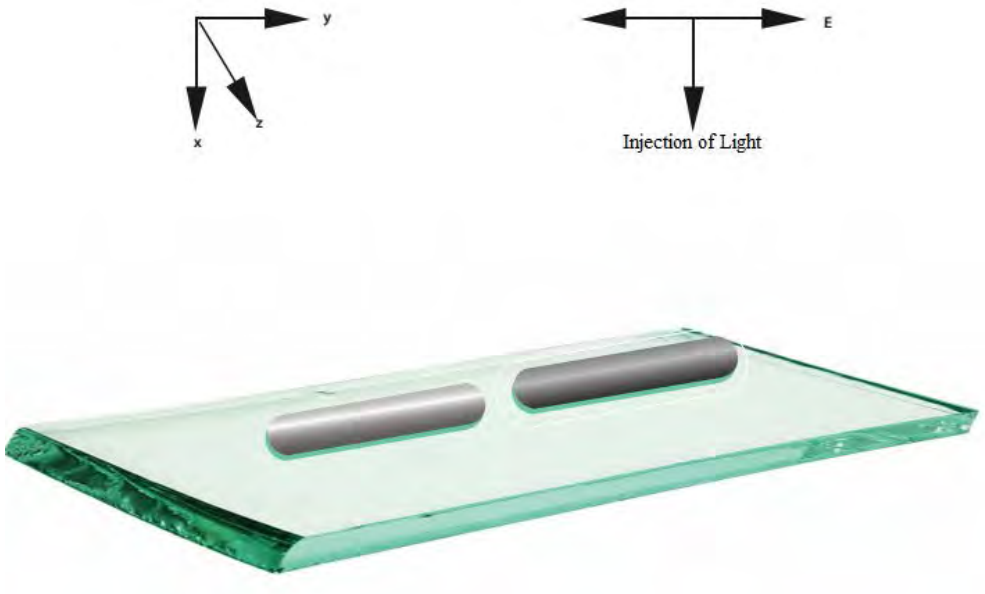

Figure 4.9: *Illustration of Injection of Light onto Structure*

4.8 Power Absorption (Advanced)

This is the advanced version of power absorption. Power absorption is taken into account so that we can observe the amount of power absorbed after the simulation is done in a graphical format. In order to access this feature, we go to "Analysis > Optical Power > Power absorbed (advanced)".

Once we go to edit the settings of this analysis we can see the various scripts that govern this analysis. This analysis returns the fraction of power from the source that is absorbed within the volume. The absorption is calculated using the following relation:

*L=0.5*eps0*w*(abs(E))^2*imag(eps))*

To provide a more accurate answer, the absorption is calculated from each field component before doing the spatial interpolation to standard mesh cell locations. It outputs three things: Pabs, Pabs_total and f. Pabs is the power absorbed per unit volume at each position (x, y, z, f). Pabs_total is the total power absorbed within the monitor (f) and f is the simply the array of frequencies of light that the analysis is run against that comes from the source that we have set up previously.

Once again we have to set up the geometry region for the analysis to run. This geometry is also setup closely to the likes of the mesh geometry.

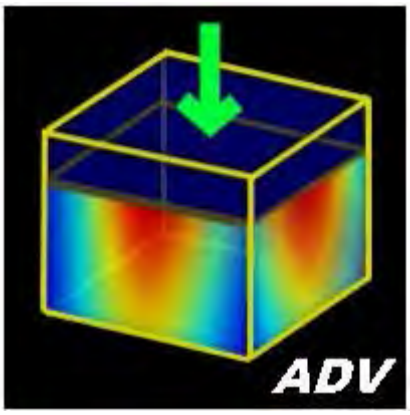

Figure 4.10: *Pabs (Advanced) logo*

4.9 Monitor

We went to “Monitor > Frequency – domain field and power”. This object is then edited. The “override global monitor settings” is checked out. This allows us to enter the value of frequency points. We change the frequency points to “use source limits” an option inbuilt within the monitor.

Then we move on to the “Geometry”. The Monitor Type is set to 2D X-normal (along the direction of the thickness of the substrate). X span automatically gets fixed to 0. If we fix the wavelength at a particular point rather than a range, Monitor gives us the electric filed or magnetic field pictures. We can even tweak the “Data to record” settings to select either electric field or magnetic field pictures or both if needed.

4.10 Summary

The software used in our simulation is FDTD Solutions by Lumerical. Lumerical develops photonic simulation software and tools. These tools help product designers to understand light, and predict how it behaves within complex circuits, structures and systems. Photonics is the study of light and its interaction with matter, and it unravels many opportunities for the world's leading technology companies across various fields including biotechnology, data communications, information storage, solar energy, environmental sensing and consumer electronics.

Among various products from Lumerical we have used the FDTD Solutions to simulate the structure and system we wanted to for our thesis. We have accurately designed our nanorods, its surroundings, substrate material, direction of incident light and electric field properties. The "Rounded Cylinder" option which was built-in helped us create our nanorods and also helped in varying the lengths, adjusting the material and its refractive index to our desired values. We used the "Rectangle" formation to create our Glass (SiO_2) substrate that our nanorods will be sitting on. The FDTD options was used to set up the surroundings of our structure and simulate the different samples and analytes that the sensor chip had to be submerged in. Within this option we had to fix the geometry of the surroundings, the boundary conditions. As the light source the TFSF source was used and its direction of injection and wavelengths was varied within this option too. A mesh analysis region was set up so that the software knew which parts of this structure needed to be simulated and calculated for and the frequency of points in the 3D space it needed to do the Maxwell equation solving to get a smooth curve. Lastly, we set up a monitor and an analysis tool named P_{abs} (Advanced) in order to see our results of light power absorbed within the area while the monitor gave us the graphical representation of electric field.

5. Simulation and Result Analysis

5.1 Introduction

Once the structure and its surroundings were set up properly we begin to run the simulations while varying different variables we deemed necessary to get the most sensitive configuration of the structure. We also tested the baseline configuration through different refractive indexes to measure the sensitivity in respect to the primary peak and the dip in the P_{abs} curve. Lastly, we measured our most sensitive configuration on refractive indexes of different real life biomolecules found in the human body.

The results obtained from our simulations have been categorized into six parts:

- Ag Nanorod Length.
- Al Nanorod Length.
- Gap Distance.
- Refractive Index Change.
- Sensitivity of Peak and Dip.
- Sensitivity on Biomolecules.

First the method of getting a P_{abs} vs. Wavelength graph has to be described. Once the all the values have been set and the simulation finishes we get to visualize the graph from the Pabs (Advanced) analysis. Then the 802 points of data is taken into script and converted into a MATLAB file. The same is done for the frequency of incident light. In MATLAB the frequency is converted to wavelength and then graphed against the power absorbed array imported from FDTD Solutions.

5.2 Ag Nanorod Length

The baseline configuration of our structure was a Ag nanorod length of 200 nm, Al nanorod length of 142 nm and the distance between them 10 nm. In the first step of our process we decided to change the Ag nanorod lengths while keeping the distance and Ag rod length constant. The lengths that were considered are: 170 nm, 180 nm, 190 nm, 200 nm, 210 nm, 220 nm, 230 nm. The results that were found (Primary Peak Wavelength, Fano Dip Wavelength, Secondary Peak Wavelength) are displayed below.

Table of Results:

Ag nanorod lengths (nm)	Primary Peak Wavelength (nm)	Fano Dip Wavelength (nm)	Secondary Peak Wavelength (nm)
170	537.6	571.7	662.0
180	553.1	588.1	673.3
190	567.4	605.1	669.3
200	580.2	621.4	686.7
210	594.3	639.9	706.0
220	606.7	659.1	715.5
230	617.5	676.4	727.7

Graphical Presentation:

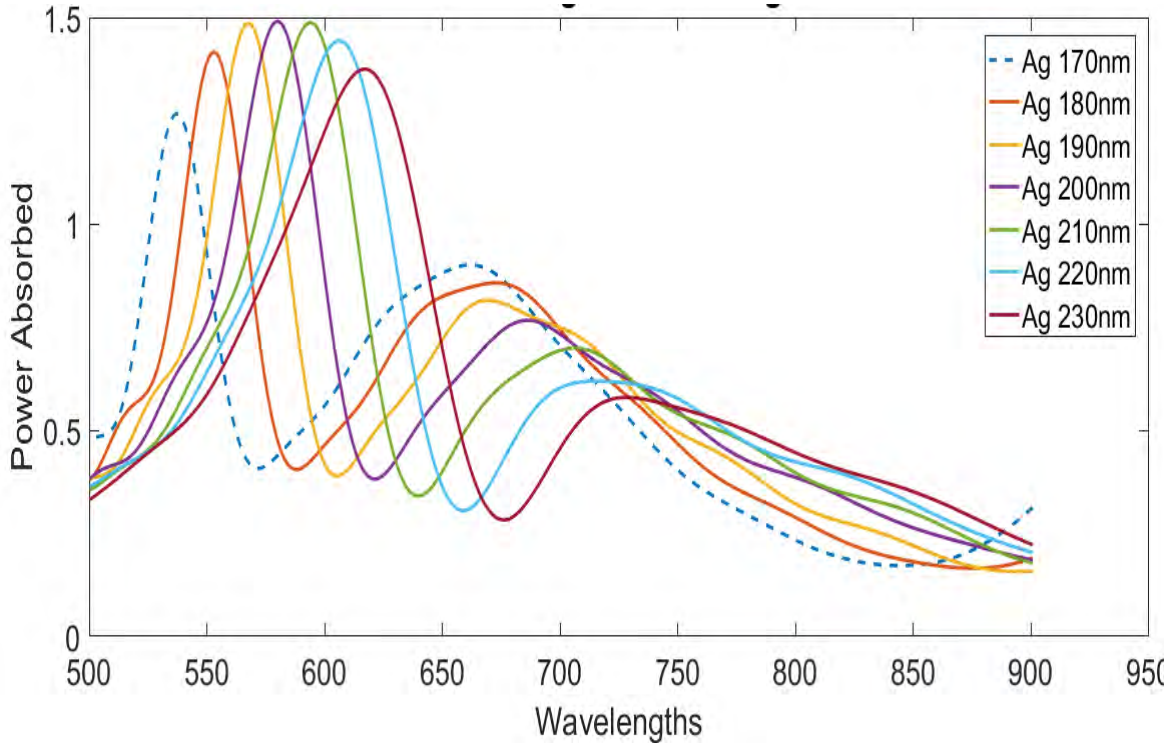

Figure 5.1:*Different Ag Nanorod Lengths*

When increasing the length of the long Ag nanorod from 170 to 230 nm with fixing the short Al nanorod length at 142 nm, the long wavelength resonant secondary peak intensity relative to the Fano dip significantly decreases while the short wavelength one gently increases. In addition, the bandwidth of the long wavelength resonant peak largely broadens while the short wavelength one slightly narrows. The primary peak rises until 200 nm length and then decreases again but with a dip that also decreases with it. The dip gets wider across the x axis as the length of the Ag nanorod increases. From this we take the 200 nm variant of the Ag nanorod length as the best configuration for sensitivity as that gives us the highest primary peak while having a low enough full width at half maximum for the dip.

5.3 Al Nanorod Length

The baseline configuration for the Al nanorod is 142 nm. We decrease and increase the length of the Al nanorod while keeping the Ag nanorod length at 200 nm and run the simulations. It is important to keep the distance between the nanorods at 10 nm. The lengths considered for the Al nanorod are: 132 nm, 142 nm, 152 nm, 162 nm, 172 nm. The results that were found (Primary Peak Wavelength, Fano Dip Wavelength, Secondary Peak Wavelength) are displayed below.

Table of Results:

Al Nanorod Lengths (nm)	**Primary Peak Wavelength (nm)**	**Fano Dip Wavelength (nm)**	**Secondary Peak Wavelength (nm)**
132	572.1	619.7	667.8
142	579.1	621.8	687.2
152	588.1	624.8	717.8
162	593.9	627.8	720.7
172	597.5	629.2	750.7

Graphical Representation:

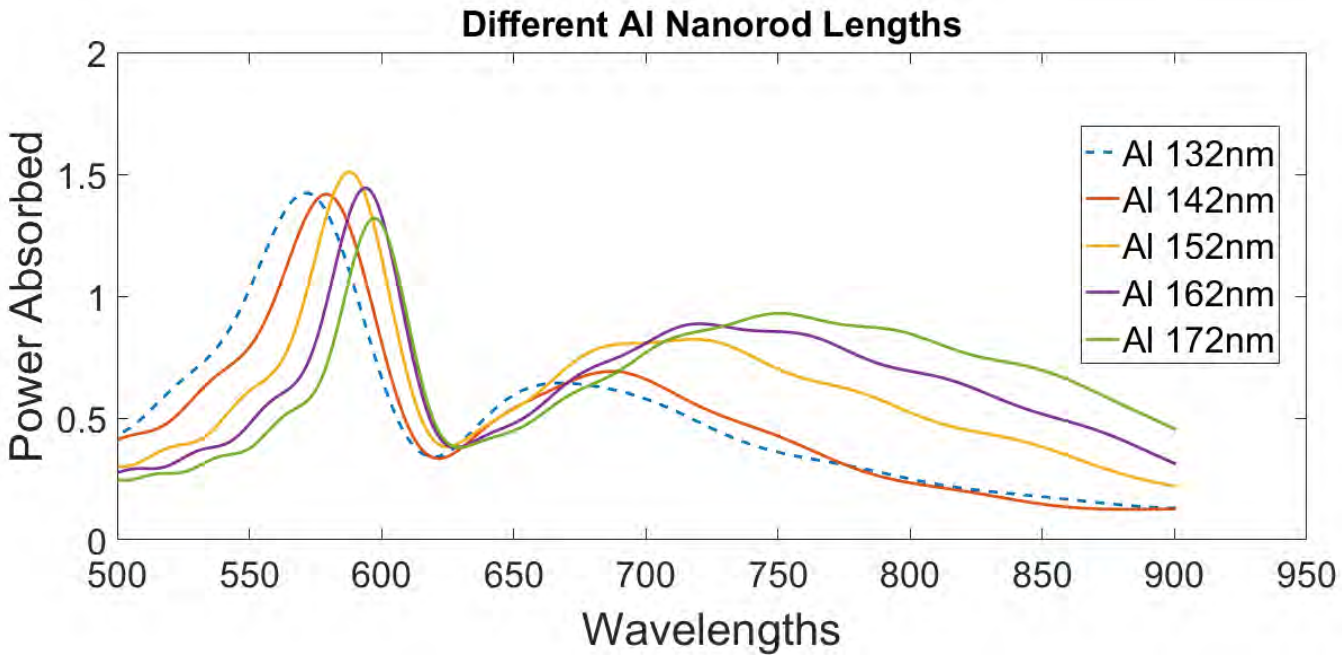

Figure 5.2: *Different Al Nanorod Lengths*

As the length of the short Al nanorod increases from 132 to 192 nm with fixed length of Ag nanorod of 200 nm, the long wavelength resonant peak intensity relative to the Fano dip significantly increases while the short wavelength one gently decreases. In addition, the bandwidth of the long wavelength resonant peak largely broadens while the short wavelength one slightly narrows. We get the highest primary peak at the 152 nm Al nanorod length and then the peak decreases but the bandwidth of the primary peak shortens. The secondary peak increases as the Al nanorod length increases but the bandwidth broadens so the peak flattens out in respect to itself. The Fano Dip gets the deepest at 152 nm length in respect to the primary peak but in respect to the secondary peak it keeps getting deeper as the length increases. We choose the 152 nm length variant the most sensitive configuration for its highest primary peak and while having a pretty short bandwidth for the secondary peak and the fano dip.

5.4 Gap Distance

The baseline configuration has the distance between the two nanorods sitting at 10 nm. We did not consider decreasing the distance between the nanorods as in a real sensor chip that space has to be kept for ligands to operate. We considered increasing the gap between the nanorods but not to the point where they would stop producing a fano dip in the absorption cross section. So, the gap distances considered are: 10 nm, 20 nm, 30 nm. In this case the Ag nanorod length has been kept at a constant 200 nm and the Al nanorod length has been kept at a constant 142 nm. The results found are displayed below.

Table of Results:

Gap Distances (nm)	**Primary Peak Wavelength (nm)**	**Fano Dip Wavelength (nm)**	**Secondary Peak Wavelength (nm)**
10	579.4	621.8	686.7
20	584.7	619.7	676.9
30	588.9	620.5	671.8

Graphical Representation:

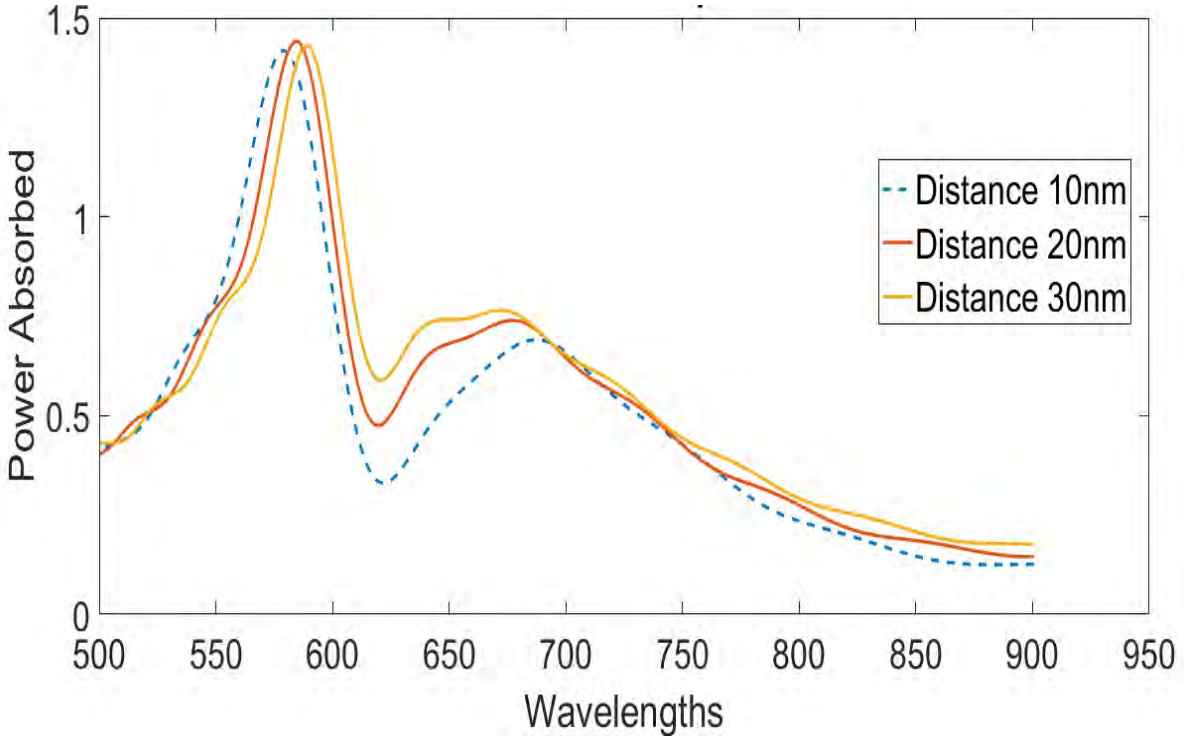

Figure 5.3:*Gap Changes*

As we can see in the graphical representation, as the distance between the nanorods are increased the fano effect dies out as the fano dip gets shallower and the secondary peaks flattens out. So, the 10 nm gap distance is chosen as the most sensitive configuration.

5.5 Refractive index change

The baseline configuration of Ag nanorod is 200 nm in length and Al nanorod being 142 nm in length while the gap distance between them is kept at 10 nm. At this configuration we run our sensor structure under different refractive indexes. We do this by changing the settings of its surroundings through the FDTD option. As a change of refractive index in surrounding environment is supposed to shift the SPR wavelength which is the main method of detection when it comes to biomolecular detection in LSPR, we test this by first doing a test with a refractive index of 1.33 which represents water or a buffer solution and then increase it up to 1.5

to see the shift in SPR wavelength. The values we considered are 1.33, 1.38, 1.40, 1.42, 1.45, 1.47, 1.5. The results that were found are listed below.

Table of Results:

Refractive Index	**Primary Peak Wavelength (nm)**	**Fano Dip Wavelength (nm)**	**Secondary Peak Wavelength (nm)**
1.33	579.1	621.8	686.7
1.38	593.7	636.8	703.8
1.40	599.1	642.6	711.6
1.42	605.6	648.6	714.4
1.45	614.2	657.6	724.7
1.47	620.1	663.4	731.2
1.5	629.2	672.8	742.0

Graphical Representation:

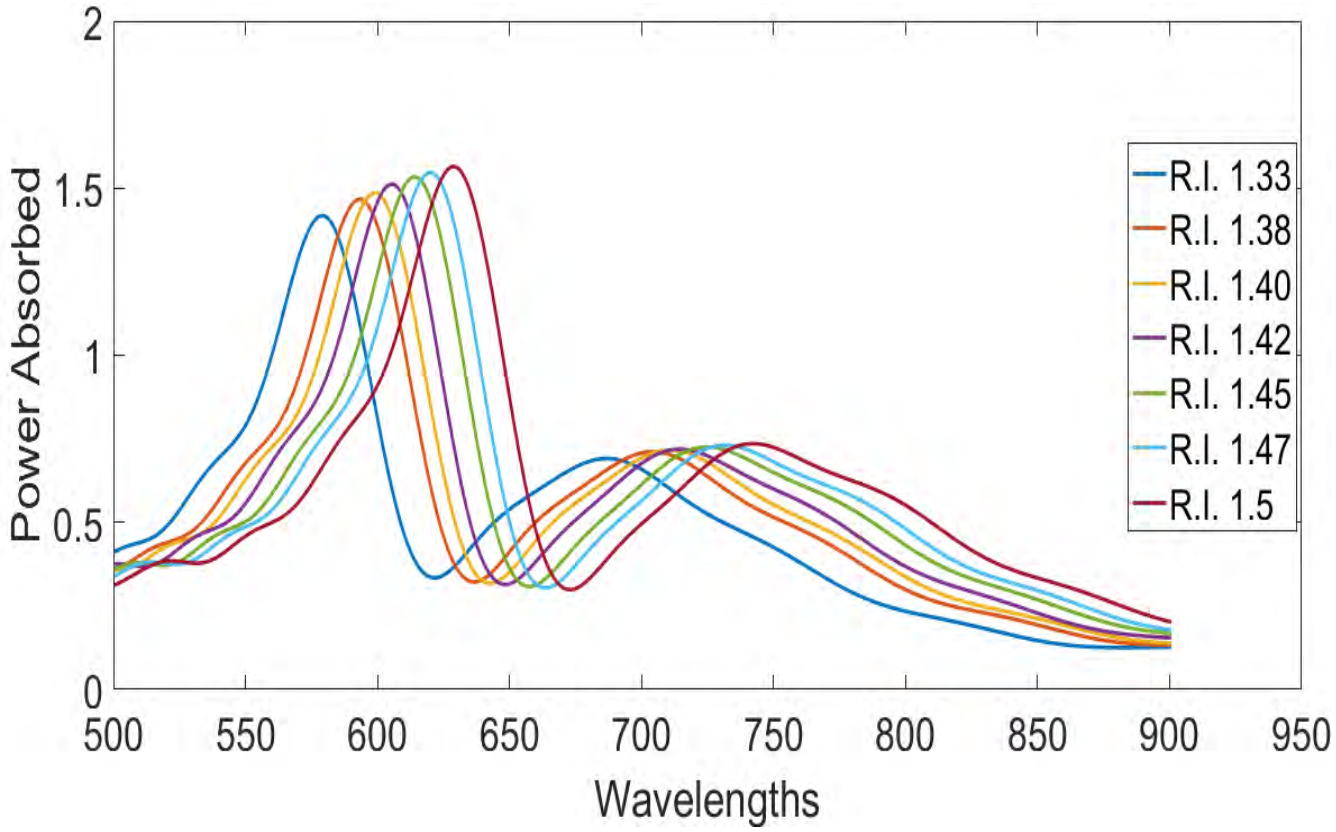

Figure 5.4: *Different Refractive Indexes*

The test with refractive index shows a very steady shift in SPR wavelengths for a steady increase in refractive index. This proves the baseline configuration of our analyzed sensor structure is sensitive to refractive index changes in its environment. In a real life situation this would relate to a sample of analytes being flown over the sensor surface and the sensor having a shift in the SPR wavelength as a reaction to the samples. The shift in the primary peak and the fano dip are more significant than the shift in the secondary peak.

5.6 Sensitivity in Peak and Dip

The objective of this part of the research is to understand how the sensitivity of the Primary Peak and the Fano Dip, and how the SPR shift vary with the change of its surrounding medium. These are obtained by using substances of different refractive indexes. Here, water is used as the control medium and the variation is recorded with respect to water. The effect of different refractive indexes was described in the section above and here the sensitivity analysis will be done.

Sensitivity is calculated from the following formula:

$$Sensitivity = \frac{d\lambda}{dn}$$

Where, dλ = Change in wavelength of incident light

dn = Change in refractive index

In this part, we shall observe the sensitivity analysis of

- Primary Peak of $\mathbf{P_{abs}}$ Curve
- Fano Dip of $\mathbf{P_{abs}}$ Curve

5.6.1 Primary Peak of P_{abs} Curve

For this sensitivity analysis the length of the Ag nanorod was fixed at 200 nm, the length of the Al nanorod was fixed at 142 nm and the distance between the nanorods was fixed at 10 nm. Both nanorods had a radius of 20 nm and the end points of the nanorods had a radius of 20 nm as well.

Below a table of results including the different refractive indexes and the wavelength the primary peak was found at for those refractive indexes are included. As well as the SPR shifts found for the refractive indexes are mentioned.

Table of Results:

Refractive Index, n	**Wavelength (nm) (λ)**	**SPR Shift (nm) (dλ)**
1.33	579.1	00.0
1.38	593.7	14.6
1.40	599.1	20.0
1.42	605.6	26.5
1.45	614.2	35.1
1.47	620.1	41.0
1.50	629.2	50.1

GraphicalRepresentation:

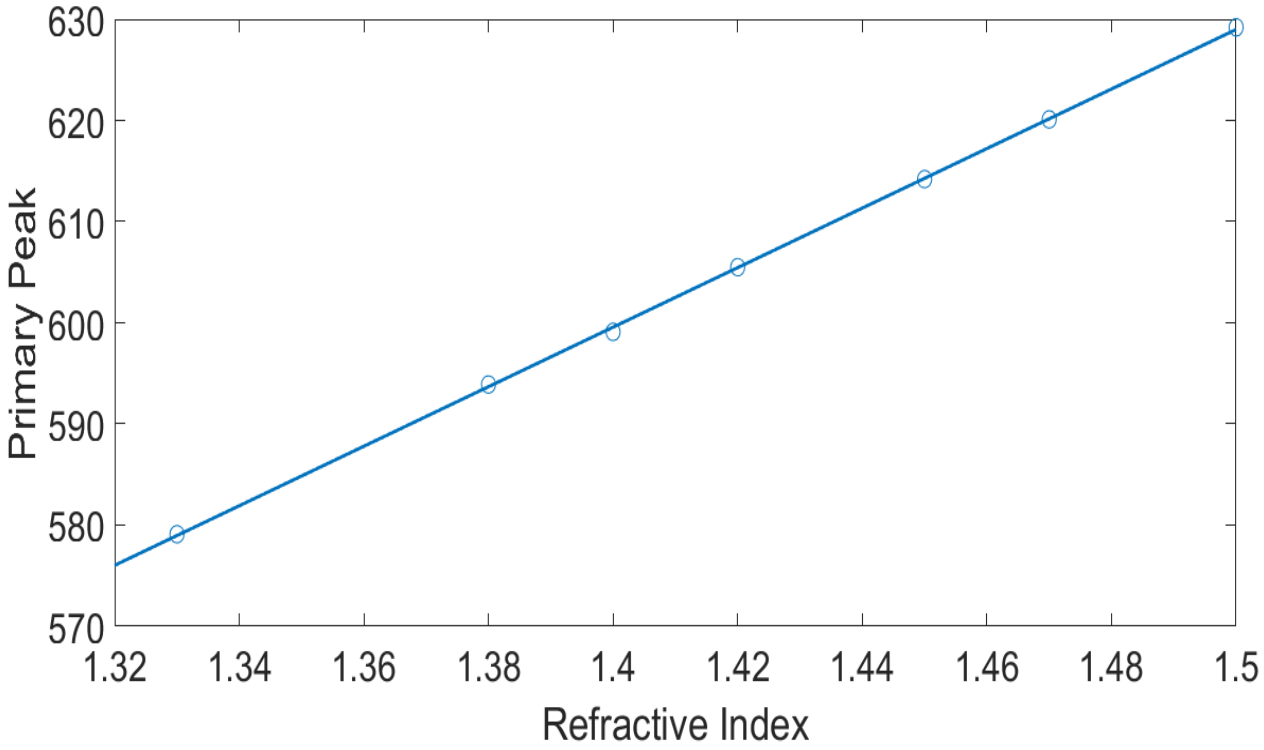

Figure 5.5: *Primary Peak Sensitivity*

Calculation:

From the slope of the line the sensitivity can be calculated as,

$$Sensitivity = \frac{d\lambda}{dn}$$

$Sensitivity$ = (605.6−593.7) ÷ (1.42−1.38) = **297.5**

5.6.2 Fano Dip of P_{abs} Curve

For this sensitivity analysis the length of the Ag nanorod was fixed at 200 nm, the length of the Al nanorod was fixed at 142 nm and the distance between the nanorods was fixed at 10 nm. Both nanorods had a radius of 20 nm and the end points of the nanorods had a radius of 20 nm as well.

Below a table of results including the different refractive indexes and the wavelength the fano dip was found at for those refractive indexes are included. As well as the SPR shifts found for the refractive indexes are mentioned.

Table of Results:

Refractive Index, n	**Wavelength (nm) (λ)**	**SPR Shift (nm) (dλ)**
1.33	621.8	0
1.38	636.8	15.0
1.40	642.6	20.8
1.42	648.6	26.8
1.45	657.6	35.8
1.47	663.4	41.6
1.50	672.8	51.0

Graphical Representation:

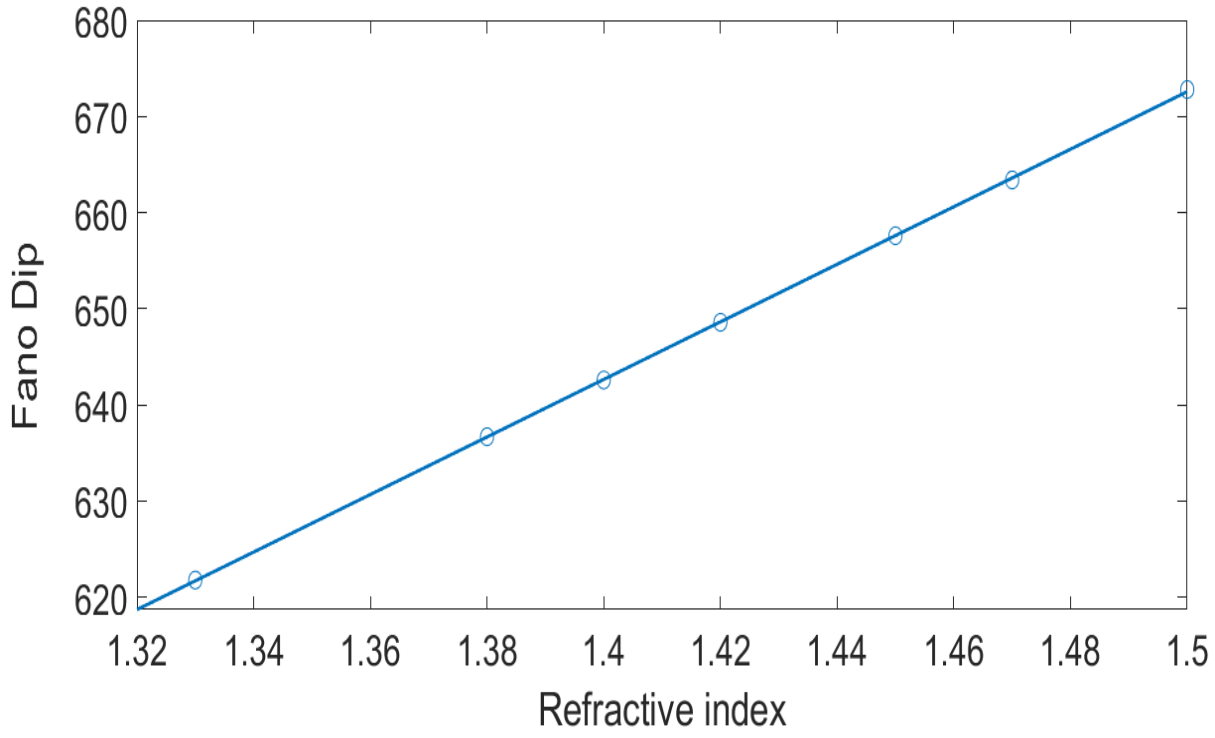

Figure 5.6: *Sensitivity of Fano Dip*

Calculation:

From the slope of the line the sensitivity can be calculated as,

$$Sensitivity = \frac{d\lambda}{dn}$$

$Sensitivity$ = (648.6−636.8) ÷ (1.42−1.38) = **295**

After analyzing the sensitivity for the primary peak and the fano dip of our sensor structure, the results seems apparent that the primary peak is more sensitive to change of refractive index in the environment than the fano dip. Nonetheless, the fano dip itself is very sensitive on its own can very well be used as a method of measurement in a real sensor.

5.7 Sensitivity on Biomolecules

The structure of the adsorbing layers of native and denatured proteins (fibrinogen, immunoglobulin, albumin, and lysozyme) was studied on hydrophilic TiO2 surface using the quartz crystal microbalance with dissipation and optical waveguide light mode spectroscopy techniques. The density and the refractive index of the adsorbing protein layers could be determined from the complementary information provided by the two in situ instruments. We take data on refractive index of four proteins in different densities on different materials and run the data against our sensor structure to see its sensitivity and SPR shift for real life biomolecules. The proteins are in three conditions:

- 80 micrograms/mL, on TiO_2
- 40 micrograms/mL, on TiO_2
- 6m Urea, on TiO_2

The refractive indexes found for these conditions and densities are given below.

Refractive Index of Proteins:

Protein	**80 micrograms/mL, on TiO_2**	**40 micrograms/mL, on TiO_2**	**6m Urea, on TiO_2**
Lysozyme	1.475	1.495	1.48
HSA	1.415	1.445	1.41
Immunoglobulin	1.415	1.41	1.42
Fibrinogen	1.405	1.40	1.43

We run all these different conditions of refractive indexes in our simulation and took the data of primary peak and the fano dip for each one. Then we measured the shift of the peak and the dip against the peak and shift found from our control medium or water with a refractive index of 1.33. The shifts found in the results are displayed below.

Shift of Primary Peak ($d\lambda_p$) in nanometers:

Protein	**80 micrograms/mL, on TiO_2**	**40 micrograms/mL, on TiO_2**	**6m Urea, on TiO_2**
Lys	49.6	56.3	51.4
HSA	32.6	41.4	31.3
IgG	32.6	31.3	33.8
Fb	29.7	28.4	37.2

Shift of Fano Dip ($d\lambda_d$) in nanometers:

Protein	**80 micrograms/mL, on TiO_2**	**40 micrograms/mL, on TiO_2**	**6m Urea, on TiO_2**
Lys	45.1	51.0	46.5
HSA	27.3	35.8	25.4
IgG	27.3	25.4	29.6
Fb	25.4	23.6	32.5

The shifts of both the peak and the dip show a promising result for a good selectivity and detection using the sensor structure used in our thesis. The shifts in the primary peak are more prominent but the fano dip shifts are very significant as well. This abides by the sensitivity analysis done by us in the section before this.

5.8 Summary

In this chapter we have described the different variables we took from our structure and how we changed them to get better selectivity out of it. And at the end we discussed our results on the sensitivity analysis of our structure and the sensitivity it can show against real life biomolecules

First the lengths of the Ag nanorod was changed into eight different values which gave us different shifts and changes in the primary peak and the fano dip and among those we chose the 200 nm length as the most sensitive configuration for its deep fano dip and highest primary peak

Then we changed the length of the Al nanorod and it showed a broadening of the bandwidth of the secondary peak with the increase of the rod length. We chose the 152 nm length of the Al nanorod as the most sensitive configuration as a min-max of primary peak height and secondary peak bandwidth. We also changed the gap distance to show that as the gap increases the fano dip starts to rise and the fano resonance phenomenon decreasing.

We also tested our structure through different refractive indexes to show the shift of the peaks and the dip as a proportional to the refractive index. From that we could also measure the sensitivity of the primary peak and the fano dip which showed the primary peak as the most sensitive detection method.

Finally the sensor structure was tested against real data of four different proteins found in the human body. This test showed us a significant SPR shift which is very promising for detection from samples in real life scenarios. Overall, this chapter has proved the validity of our structure in terms of sensitivity and selectivity as a biomolecule detector.

6. Conclusion

This paper was done in the hopes of pursuing the unique characteristics of Localized Plasmon Resonance (LSPR) in colloidal nanoparticles. Besides its various applications in optics, photo catalysis, medicine and photovoltaic, we have seen its application in bio-sensing. The nanoparticle structure, comprised of a Silver nanorod and a Aluminum nanorod, placed closely together on a substrate (preferably Silicon Dioxide). The setup was immersed in water and illuminated with light.

Our thesis research was based on the fanoresonance that occurred from the described setup and the fanodip found in the Absorption Cross-section curve. This fanoresonance can be widely tunable through a change in the different variables of the setup. We took Silver and Aluminum nanorod lengths, the gap between the rods.

The length variable test was done by keeping one of the nanorods at a constant length while changing the length of the other one. At first the Silver nanorod length was taken as a variable and increased and decreased. A consistent rise in the height of the primary peak along with a broadening of the bandwidth of the secondary peak and fanodip is noticed. In this test the 200 nm length was chosen as the most sensitive configuration of the variable.

The test with the Aluminum nanorod length was carried out similarly which showed a shortening bandwidth of the primary peak with increasing length. It also showed the fano dip getting shallower while the secondary peak getting wider with the increasing length. In this test the 152 nm length was chosen as the most sensitive configuration of the variable.

We tested increasing the gap distance between the two nanorods from 10 nm to 30 nm. This test proved that the further away from each other the nanorods were placed the shallower the fano dip was getting. This shows that the nanorods had to be placed closely for fanoresonance to occur.

Next, the sensitivity of the sensor structure was tested against an increasing refractive index starting from a base of 1.33 which represents water, all the way to 1.5 which represented biomolecules or proteins of heavy molecular density. This showed a proportionate increase in SPR shift with the increase of refractive index. This proves the validity of the structure as a bio detector. We found that the sensitivity of the primary peak was higher than that of the fano dip.

Lastly the structure was faced against real data collected from proteins of the human body to see how much SPR shift we could expect in real life scenarios. The shifts in both the primary peak and the fano dip were significant enough to pass a selectivity test for each of the protein’s detection.

In conclusion, optical properties of Al–Ag heterogeneous nanorod dimers are studied by theoretical simulation method. A pronounced Fano dip in the extinction spectra is observed, which strongly depends on both the geometry parameters of the complex nanostructure and the refractive index of the surrounding environment. The LSPR sensitivity of the heterogeneous metallic complex nanostructures is also checked and a sensitivity of 297.5 for the primary peak and 295 for the fano dip is obtained, which may find applications in biological sensing and molecule detection based on the coherent plasmonic coupling.

References

[1] Zhang, C., Chen, B., Li, Z., Xia, Y., & Chen, Y. (2015).Surface Plasmon Resonance in Bimetallic Core-shell Nanoparticles.*The Journal of Physical Chemistry*.doi: 10.1021/acs.jpcc.5b04232

[2] Chin, C. W., (2011). Localized Surface Plasmon Resonance with the use of Silver and Titanium Oxide Nanostructures.p. 1. Retrieved from:

http://web.utk.edu/~zzhang24/Chuck%20Chin%20Thesis.pdf

[3] Giannini, R. (1978). Shape Dependence of Localized Surface Plasmon Resonances and their application in nanoemmiters. Retrieved from:

http://e-collection.library.ethz.ch/eserv/eth:47630/eth-47630-02.pdf

[4] Stockman, M. I., (2011). Nanoplasmonics: the physics behind the applications. *Physics Today*, 39-44. Taken from:

http://physics.gsu.edu/stockman/data/Stockman_Phys_Today_2011_Physics_behind_Appl ications.pdf

[5] Maier, S. A. (2007) Localized Surface Plasmons. *Plasmonics: Fundamentals and applications*,p.65-72.

From:https://www.londonnano.com/sites/default/files/uploads/research/highlights/Nanoplasmonics/pdf

[6]*Plasmonics*

Retrieved from: https://www.physik.huberlin.de/de.nano/lehre/Gastvorlesung%20Wien/plasmonics

[7]*Surface Plasmon Resonance.*

Retrieved from:

https://en.wikipedia.org/wiki/Surface_plasmon_resonance

[8] Raether, H. (1988). Surface Plasmons on Smooth and Rough Surfaces and on Gratings.*Springer TractsinModernPhysics*, Vol. 111, Springer Berlin

[9] Localized Surface Plasmon Resonance Theory. *Localized Surface Plasmon Resonance vs. Surface Plasmon Resonance*. Retrieved from: https://nicoyalife.com/technology/surfaceplasmon-resonance/localized-surface-plasmon-resonance-theory/

[10] Free electron model (2016).

Retrieved from: https://en.wikipedia.org/wiki/Free_electron_model

[11] Biomolecule (2016).

Retrieved from: https://en.wikipedia.org/wiki/Biomolecule

[12] Lysozyme (2016).

Retrieved from: https://en.wikipedia.org/wiki/Lysozyme

[13] Human Serum Albumin (2016).

Retrieved from: https://en.wikipedia.org/wiki/Human_serum_albumin

[14] Immunoglobulin G (2016).

Retrieved from: https://en.wikipedia.org/wiki/Immunoglobulin_G

[15] About Lumerical. *lumerical*.

Retrieved from: https://www.lumerical.com/company/about_lumerical.html

[16] PDB-101: Lysozyme.

Retrieved from:

https://www.google.com/search?q=lysozyme&client=firefox-bab&source=lnms&tbm=isch&sa=X&ved=0ahUKEwiy3oS81-rQAhUBVhQKHf5eBJoQ_AUICSgC&biw=1366&bih=657#imgrc=J0_6P2nRKcicaM%3A

[17] Immunoglobulin G. Causes, symptoms, treatment Immunoglobulin G.

Retrieved from:

https://www.google.com/search?q=immunoglobulin+g&client=firefox-bab&source=lnms&tbm=isch&sa=X&ved=0ahUKEwia1KqJ2OrQAhVLthQKHca6D5cQ_AUICCgB&biw=1366&bih=657#imgrc=3CSnlav6ZTO0eM%3A

[18] Entertainment - Home Page.

Retrieved from:

https://www.google.com/search?q=transmission+electron+microscope&client=firefox-bab&source=lnms&tbm=isch&sa=X&ved=0ahUKEwjq4sqK2erQAhVFXhQKHcpuBJUQ_AUICCgB&biw=1366&bih=657#tbm=isch&q=transmission+electron+microscope+images+of+nanoparticles&imgrc=GioadFCbmkDLhM%3A

[19] Scanning Electron Microscope.

Retrieved from:

https://www.google.com/search?q=transmission+electron+microscope&client=firefox-bab&source=lnms&tbm=isch&sa=X&ved=0ahUKEwjq4sqK2erQAhVFXhQKHcpuBJUQ_AUICCgB&biw=1366&bih=657#tbm=isch&q=scanning+electron+microscope+images&imgrc=Ncm1bbJJJ40UYM%3A

[20] Lumerical Solutions, Inc.

Retrieved from:

https://www.google.com/search?q=lumerical+solutions+logo&client=firefox-bab&source=lnms&tbm=isch&sa=X&ved=0ahUKEwjmxIj54-rQAhWFORoKHfhRBw4Q_AUICCgB&biw=1366&bih=657#imgrc=3iyJWdEBdavy3M%3A

[21] J. Fan, C. Wu, K. Bao, J. Bao, R. Bardhan, N. Halas, V. Manoharan, P. Nordlander, G. Shvets, F. Capasso (2010).Self-assembled plasmonic nanoparticle clusters.*Science*. 2010 May 28;328(5982):1135-8. doi: 10.1126/science.1187949.

Retrieved From:

https://www.ncbi.nlm.nih.gov/pubmed/20508125

[22] Periodic boundary conditions.

Retrieved from:

https://kb.lumerical.com/en/index.html?ref_sim_obj_symmetric_anti-symmetric.html

[23] XuetingCi, Botao Wu, Min Song, Yan Liu, Gengxu Chen, E. Wu, HepingZeng. Tunable Fano resonances in heterogenous Al–Ag nanorod dimers.*Appl. Phys A.*doi: 10.1007/s00339-014-8479-z

[24] Mesh refinement.

Retrieved from:

https://kb.lumerical.com/en/index.html?ref_sim_obj_symmetric_anti-symmetric.html

[25] Wilson, W. L., Szajowski, P. F. &Brus, L. E. (1993). Quantum confinement in sizeselected surface-oxidized silicon nanocrystals.*Science* 262, 1242-1244.

[26] Durisic, N., Godin, A. G., Walters, D., Grutter, P., Wisemann, P. W. &Heyes, C. D. (2011). Probing the "dark" fraction of core-shell quantum dots by ensemble and single particle pH-dependent spectroscopy.*ACS Nano* 5, 9.62-9073.

[27] Verberk, R., Chon, J. W. M., Gu, M. &Orrit, M. (2005). Environment dependent blinking of single semiconductor nanocrystals and statistical aging of ensembles.*Physics E* 26, 19-23.

[28] Issac, A., Borczyskowski, C. &Cichos, F. (2005). Correlation between photoluminescence intermittency of CdSe quantum dots and self-trapped states in dielectric media.*Phys Rev*. B 71, 161302 (R).

[29] Bohren, C. F. & Huffman, D. R. (2004). Absorption and scattering of light by small particles. Wiley, Weinheim

[30] Prodan, E., Radloff, C., Halas, N. J. & Norlander, P. (2003). A hybridization model for the plasmon resonance of complex nanostructures.*Science 302*, 419-422.

[31] Klar, T. A. &Feldmann, J. (2012). Complex-shaped metal nanoparticles: Bottom-up syntheses and applications. Edited by Sau, T. K. &Rogach, A. L. Viley, chapter 12

[32] Lakowicz, J. R. (2005). Radiative decay engineering 5: Metal-enhanced fluorescence and plasmon emission. *Anal.Biochem*. 337, 171-194.

[33] Anker, J. N., Hall, W. P., Lyandres, O., Shah, N. C., Zhao, J. & Van Duyne, R. P. (2008). Biosensing with plasmonic nanosensors.*Nature Materials* 7, 442-453.

[34] Malinsky, M. D., Kelly, K. L., Schatz, G. C. & Van Duyne, R. P. (2001). Chain length dependence and sensing capabilities of the localized surface plasmon resonance of silver nanoparticles chemically modified with alkanethiol self-assembled monolayers. *J. Am. Chem*. Soc.123, 1471-1482.

[35] Willets, K. A. & Van Duyne, R. P. (2007). Localized Surface Plasmon Resonance Spectroscopy and Sensing.*Annu Rev. Phys. Chem.* 58, 267-297.

[36] Khalavka, Y. Becker, J. &Sönnichsen, C. (2009). Synthesis of rod-shaped gold nanorattles with improved plasmon sensitivity and catalytic activity.*JACS* 131, 1871- 1875.

[37] Kravets, V. G., Schedin, F., Kabashin, A. V. &Grigorenko, A. N. (2009). Sensitivity of collective plasmon modes of gold nanoresonators to local environment. *Opt. Lett*. 35, 956- 958.

[38] Pillai, S., Catchpole, K. R., Trupke, T. & Green, M. A. (2007). Surface plasmon enhanced silicon solar cells. *J. Appl. Phys*. 101, 093105.

[39] Smith, D. R., Pendry, J. B. & Wiltshire, M. C. K. (2004). Matamaterials and negative refractive index.*Science*. 305, 788-792.

[40] Li, D., Qin, L., Qi, D. X., Gao, F., Peng, R. W., Zou, J., Wang, Q. J. & Wang, M. (2010). Tunable electric and magnetic resonances in multilayered metal/dielectric nanoplates at optical frequencies. J. Phys. D: *Appl. Phys*. 34,345102.

[41] Barnes, W. L. (2006). Surface plasomn-polariton length scales: A route to subwavelength optics. J. *Opt. A: Pure Appl*. Opt. 8, S87-S93

[42] Maier, S. A., Kik, P.G. Atwater, H. A., Meltzer, S. Harel, E. Koel, B. E. &Requicha, A. A. A. G. (2003). Local detection of electromagnetic energy transport below the diffraction limit in metal nanoparticle plasmon waveguides. *Nature* 2, 229-232.

[43] Ozbay, E. (2006). Merging photonics and electronics at nanoscale dimensions.*Science* 311, 189-193.

[44] Walters, R. J., van Loon, R. V. A., Brunets, I., Schmitz, J. &Polman, A. (2010). A silicon-based electrical source of surface plasmon polaritons. *Nature Materials* 9, 21-25.

[45] Ringe, E., Langille, M. R., Sohn, K., Zhang, J., Mirkin, C. A., van Duyne, R. P. & Marks, L. D. (2012). Plasmon length: A universal parameter to describe size effects in gold nanoparticles.

[46] Ringe, E., Zhang, J., Langille, M. R., Mirkin, C. A., Marks, L. D., van Duyne, R. P. (2012). Correlating the structure and localized surface plasmon resonance of single silver right bipyramids.*Nanotech* 23, 444005.

[47] Myroshnychenko, V., Rodriguez-Fernandez, J. R., Pastoriza-Santos, I., Funston, A.M., Novo, C., Mulvaney, P., Liz-Marzan, L. M. & Garcia de Abajo, F. J. (2008). Modelling the response of gold nanoparticles.*Chem. Soc. Ref*. 37, 1792.

[48] Temple, T. L. &Bagnall, D. M. (2011). Optical properties of gold and aluminium nanoparticles for silicon solar cell applications.*J. Appl. Phys*. 109, 084343.

[49] Knight, M. W., Wu, Y., Lassiter, J. B. & Halas, N. J. (2009). Substrate matter: Influence of an adjacent dielectric on an individual plasmonic nanoparticle. *Nano Lett*. 9, 2188- 2192.

[50] Vernon, K. C., Funston, A. M., Novo, C., Gomez, D. E., Mulvaney, P. & Davis, T. J. (2010). Influence of particle-substrate interaction on localized plasmon resonances. *Nano Lett*. 10, 2080-2086.

[51] Noguez, C. (2007). Surface plasmons on metal nanoparticles: the influence of shape and physical environment. *J. Phys. Chem*. C 111, 3806-3819.

[52] Kelly, K. L., Coronado, E., Zhao, L. L. & Schatz, G. C. (2003). The optical properties of nanoparticles: The influence of size, shape, and dielectric environment. *J. Phys. Chem*. B 107, 668-677.

[53] Ming, T., Zhao, L., Yang, Z., Chen, H., Sun, L., Wang, J. & Yan, C. (2009). Strong polarization dependence of plasmon-enhanced fluorescence on single gold nanorods. *Nano Lett*. 9, 3896-3903.

[54] Thompson, P. G., Biris, C. G., Osley, E. J., Gaathon, O., Osgood Jr., R. M., Panoiu, N. C. & Warburton, P. A. (2011). Polarization-induced tunability of localized surface plasmon resonances in arrays of sub-wavelength cruciform apertures.*Opt. Express* 19, 25035- 25047.

[55] Kooij, E. S. &Poelsema, B. (2006). Shape and size effects in the optical properties of metallic nanorods.*Phys, Chem. Chem. Phys*. 8, 3349-3357.

[56] Kooij, E. S., Ahmed, W., Zandvliet, H. J. W. &Poelsema, B. (2011). Localized surface plasmons in noble metal nanospheroids. *J. Phys. Chem*. C 115, 10321-10332.

[57] Sönnichsen, C., Franzi, T., Wilk, T., von Plessen, G &Feldmann, J. (2002). Drastic reduction of plasmon damping in gold nanorods. Phys, Rev. Lett. 88, 077402.

[58] Zoric, I., Zach, M., Kasemo, B., &Langhammer, C. (2011).Material independence, subradiance, and damping mechanisms.*ACS Nano* 5, 2535-2546.

[59] Sönnichsen, C., Franzl, T., von Plessen, G. &Feldmann, J. (2002). Plasmon resonances in large noble-metals clusters. *New Journal of Physics* 4, 93.1-93.8.

[60] (2000). Light scattering by nonspherical particles.Edited by Mishchenko, M. I., Hovenier, J. W. & Travis, L. D., Academic Press.

[61] Novotny, L. & Brecht, B. (2006). Principles of nano-optics. University Press, Cambridge.

[62] Hohenester, U. &Krenn, J., (2005). Surface plasmon resonances of single and coupled metallic nanoparticles: A boundary integral method approach. *Phys. Rev. B* 72, 195429.

[63] Berkovitch, N., Ginzburg, P. & Orenstein, M. (2012). Nano-plasmonic antennas in the near infrared regime.*J. Phys.: Condens. Matter* 24, 073202.

[64] Mock, J. J., Barbic, M., Smith, D. R., Schultz, D. A. & Schultz, S. (2002). Shape effects in plasmon resonance of individual colloidal silver nanoparticles. *J. Chem. Phys*. 116, 6755-6759

[65] Bryant, G. W. (2008). Mapping the plasmon resonances of metallic nanoantennas.*Nano Lett*.8, 631-363.

[66]Boris luk'yanchuk1, Nikolay I. Zheludev, Stefan A. Maier, Naomi J. Halas, Peter Nordlander, Harald Giessen and Chong Tow Chong. The Fano resonance in plasmonic nanostructures and Metamaterials.*Nature Materials.*Published online: 23 August 2010.doi: 10.1038/nmat2810

[67]Fibrinogen.

Retrieved from: https://en.wikipedia.org/wiki/Fibrinogen

[68]FAQ for the Quickvet Equine Fibrinogen test.

Retieved from: https://www.smb.dk/joomla/faqs-equine-fibrinogen

[69]Firbrinogen Structure. Retrieved from:

http://www.thrombocyte.com/wp-content/uploads/2015/08/fibrinogen-levels.png

[70] David J. Smith, Chapter 1 : Characterization of Nanomaterials Using Transmission Electron Microscopy, *Nanocharacterisation (2)*, 2015, pp. 1-29 DOI: 10.1039/9781782621867-00001

[71] Brian J. Ford, David C. Joy, Savile Bradbury. Scanning electron microscopy (SEM).*Encyclopedia Britannica.*

Retrieved from: https://media1.britannica.com/eb-media/13/47113-004-EE88DE20.jpg